論文 / 著書情報
Article / Book Information

題目(和文)	
Title(English)	Computational Pathology Image Analysis Based on Nuclear Characteristics
著者(和文)	BoonsiriOranit
Author(English)	Oranit Boonsiri
出典(和文)	学位:博士(工学), 学位授与機関:東京工業大学, 報告番号:甲第10273号, 授与年月日:2016年6月30日, 学位の種別:課程博士, 審査員:長橋 宏,渡邊 澄夫,山村 雅幸,宮下 英三,長谷川 修,木賀 大介
Citation(English)	Degree:Doctor (Engineering), Conferring organization: Tokyo Institute of Technology, Report number:甲第10273号, Conferred date:2016/6/30, Degree Type:Course doctor, Examiner:,,,,,
学位種別(和文)	博士論文
Type(English)	Doctoral Thesis

Computational Pathology Image Analysis Based on Nuclear Characteristics

Oranit Boonsiri

This dissertation is submitted for the degree of

Doctor of Engineering

June 2016

Abstract

Cancer is a significant health problems around the world. Pathology is a microscopic study of tissue structure to examine disease. The nuclear properties have significant representation for cancer diagnosis. Except traditional color image, this study investigate various kinds of imaging technologies including multispectral images and 3D images to analyze cancer. These imaging systems may provide more information than traditional color image and obtain an additional option to pathologists in order to explore a new perspective. The objective of this study is to implement a computational method to describe nuclear characteristics of pathology images and classify cancer in hepatocellular carcinoma and distinguish favor benign and borderline types in thyroid follicular lesion. The proposed system mainly contains two parts. First, nuclear segmentation is performed based on pixel-based classification. Next, nuclear characteristics are represented utilizing statistical and textural features. Lastly, Bag-of-visual-word model with random forest classifier are investigated in classification step.

Dedicate to my parents ...

Acknowledgements

I greatly appreciate Professor Hiroshi Nagahashi, my supervisor for his kindness, support, constructive comments and guidance through my doctoral student's life. I would like to thank Professor Masahiro Yamaguchi for giving an opportunity to be a research assitantship at research and development project "Pathological Image Recognition" supported by the New Energy and Industrial Technology Development Organization (NEDO). I would like to extend my sincere thanks to Dr. Kimura Fumikazu and Dr. Kiyotada Washiya for their kind support, valuable comments and guidance for my entire research especially in the medical point of view.

I would like to thank Mitsubishi UFJ Bank Foundation for providing me scholarship. I also wish to thank all of my lab mates who always support me.

Lastly, my doctoral study would not have been succeeded without my family for their love and support. I would like to extend my sincere to my parents, brother and sister.

Contents

List of Figures

List of Figures

List of Tables

Chapter 1

Introduction

1.1 Objective

The visual interpretation of cancer diagnosis depends on pathologists' experiences, time consuming for analysis and various kinds of cell images. Therefore, computer aided diagnosis (CAD) systems would support pathologists to make decisions and provide useful information for clinical treatment and also helps pathologists as a pre-scanning tool. Except diagnosis perspective, the quantitative analysis based on chromatin texture in cancer cells [1] will support pathologists to explore the reason behind a specific disease identification. CAD systems are based on image analysis, pattern recognition, machine learning techniques, data visualization and human interaction. Pathology images investigation has a significant image interpretation and classification in CAD systems. These systems have some beneficial keys comparing with manual diagnosis such as consistency, reliability, efficiency for cancer diagnosis. Furthermore, medical image analysis has become an attractive topic for researchers to discover new perspective with combining pathologists point of view and computational technologies including image analysis and classification methods. However, various kinds of computational methods have been proposed in different techniques, diseases and imaging technologies. These systems is expected to be more powerful tools.

This dissertation propose computational method for describing nuclear characteristics of pathology images and classify cancer. The aim is to utilize various

kinds of imaging technologies for cancer analysis. The main goal of this research is summarized as follows.

- Defining significance of textural feature descriptors for representing nuclear characteristics.
- Defining a computational method for nuclei segmentation and classification in pathology images.
- Defining the efficiency of investigating multispectral images and volumetric data for cancer diagnosis.

1.2 Approach

Pathology is a microscopic study of tissue especially in cancer diagnosis. Subcellular components of tissue play an important role for cancer analysis. Most of cancer types are diagnosed by visualizing pathology images [1]. To diagnose cancers, pathologists use tissue samples obtained from patients via biopsy. Pathologists mainly examine tissues such as nuclei, glands and lymphocyte and discriminate them on normal, benign and malignant [2]. The morphological appearance of these structures is an important indicator for analysis. Since most of normal nuclei appear as a round or ellipsoidal shape, the sizes and morphological features of nuclei tend to be uniform. In contrast, cancer nuclei have irregular shapes, variables in size and atypia chromatin patterns [3]. Consequently, the characteristics of nuclei indicate cancerous condition.

Due to the importance of nuclear structures which has a significant interpretation for cancer analysis. In this research, we analyze liver and thyroid cancer in pathology images from nuclear characteristics. Except traditional color images which have been widely used for analysis, this study investigate other imaging technologies including multispectral images and 3D images. These imaging technologies may support a novel system and provide an additional option to pathologists to see beyond color images.

This dissertation contains two studies. These two studies diagnose different types of cancer and imaging systems. However, they have similar computational

methods. The computational method mainly contain two steps, i. nuclei segmentation based on pixel-based classification. ii. nuclear classification with BOW model.

- Study I: High-magnification of histopathological multispectral images are investigated to classify hepatocellular carcinoma (HCC). This study focus on classification of normal and HCC cell nuclei by extracting the textural properties of nuclei in multispectral images.

- Study II: We classify subclassification of thyroid follicular tumor in 3D images. The objective of this study is to classify favor benign and borderline types in follicular thyroid adenoma by utilizing volumetric data.

1.3 Contributions

The entire studies have two main topics which investigate different imaging technologies. However, these two studies have similar core framework. The contributions of this dissertation are listed as follow.

1. Classification of HCC in multispectral images.

    - Proposed parameter selection to improve classification accuracy for all multispectral bands.
    - Analyze the significance of individual multispectral bands.
    - Analyze groups of multispectral bands based on color spectrum.

2. Classification of favor benign and borderline types in FTA for volumetric data.

    - Proposed a new 3D nuclei segmentation method.
    - Analyze FTA based on statistical and textural properties of nuclei.

1.4 Outline

This dissertation is organized as follow. Chapter 2 explains related works in medical image analysis fields, including nuclear segmentation, feature extraction, classification techniques. Chapter 3 describes system overview of proposed method. The proposed system consists of two main steps which are nuclear segmentation and nuclear classification. The nuclear segmentation is performed based on pixel-based classification technique. Nuclear classification illustrates feature extractions, classification model and evaluation strategies that utilize in our system. Chapter 4 describes experimental results on classification of HCC in multispectral images. Chapter 5 presents the second study that aim to distinguish favor benign and borderline types of FTA in volumetric data. Finally, this dissertation is concluded all studies and future works in chapter 6.

Chapter 2

Related works

2.1 Introduction

Hepatic cancer is the third most frequent cause of cancer death in the world, especially in developing countries including Asia and Africa [4]. The most common type of primary hepatic cancer is Hepatocellular carcinoma (HCC). Histopathology examination is one of the techniques that use for the HCC from tissue samples that have been obtained from patient via biopsy. Pathologists discriminate normal, benign and malignant tissues by the patterns of nucleis structures [2]. HCC tumor are classified into different grade of cancer according to morphological properties of nucleus such as shape, size and chromatin pattern. Most of normal cells have similar size and rounded shape. However, cancer cells tend to have irregular shape and various size [3]. From these difference, nuclear region has a significant property to classify normal and cancer in computer aided diagnosis system.

Follicular Thyroid is one of the common type of thyroid cancer. Thyroid follicular examination get tissue sample from patient via fine needle aspiration. It is the first step for diagnosis [5]. In order to deliver effective treatment according to the risk of malignancy, indeterminate follicular neoplasm (FN) has been recommended to triage patients. The Japan Thyroid Association (JTA) categorized indeterminate FN into three levels of risk stratification as favor benign (low risk), borderline (moderate risk), and favor malignant (high risk) [6]. The favor

malignant type has high probability of 40-60 percent to be malignancy. Therefore, a patient diagnosed as favor malignant in cytological examination should be operated immediately. Furthermore, favor benign and borderline types can be observable. However, it is difficult to distinguish the difference between favor benign and borderline by visual interpretation on a given images.

2.2 Imaging technologies

The multispectral imaging technology has been extended from a remote sensing field to medical and biological fields as an effective technique for medical image analysis. Multispectral images provide spatial and spectral information. It captured in the different narrow band of wavelength in visible spectral and invisible spectral. Therefore, the information has an advantage to perform histopathological analysis and broaden pathological knowledge as a new potential [7]. Over the years, researchers have invented various multispectral imaging systems for histopathological analysis of biological tissue specimen [8–10]. These systems take advantage of using the combined spatial-spectral information to detect and classify cancer.

In medical image analysis, 3D images are become popular for researchers to explore an additional information and new perspective which aim to have a beneficial for analysis. Moreover, 3D visualization can view the organ in realistic. This point would help medical doctors to diagnosis effectively. Currently, 3D imaging technology is available to acquire 3D microscopic images, and they help pathologists and researchers to discover a new cell's property. For instance, 3D cell segmentation methods have been proposed to segment nuclei in fluorescence microscope images [11],[12] and bright field microscopic images [12].

2.3 Image segmentation

Researchers have been proposed segmentation algorithms to identify subcellular structures from multispectral images. Most of segmentation algorithms utilized both of spatial and spectral information. The pixel-based methods are widely used in multispectral and hyperspectral images for segmentation such as Spectral

Angle Mapper (SAM) [13] and Spectral Information Divergence (SID) [14]. The idea of SAM and SID techniques is to compute the spectral similarity between two spectral vectors. Guan et al. [15] applied SID algorithm in white blood cell segmentation on hyperspectral images and achieved promising result. Furthermore, conditional random field model (CRF) [16] and support vector machine (SVM) [17] were proposed to segment nuclei and other subcellular structures.

3D cell segmentation methods have been proposed to segment nuclei in fluorescence microscope images [11],[12] and bright field microscope images [12]. Moreover, 3D segmentation algorithms, such as watershed [18], gradient vector flow [11], and sliding band filter [12], well perform when a given image excludes a high level of image noises or complexities of background images.

2.4 Image classification

The region of interest can be extracted features before performing classification in order to represent region of interest effectively. The computational of feature representations are based on morphological properties and textural characteristics. In particular, feature extraction mainly contains into three categories.

- Morphological properties: area, circularity, sphericity, volume.
- Statistical measurements: average, standard deviation, maximum, minimum, energy, entropy, contrast, homogeneity.
- Texture: Gabor filter banks, Haralick, Local binary pattern.

The extracted feature from region of interest in dataset were employed to classify based on supervised learning technique. Researcher have been proposed various kinds of feature extraction techniques for representing significant characteristics in region of interest in order to improve classification accuracy.

The utility of Gabor filters have been beneficial. Particularly, Gabor filters have accomplished in many applications related to texture analysis. Gabor descriptors are the effective features to represent the characteristic of an image. Specifically, Gabor descriptors have been widely applied to medical image analysis in histopathology image.

2. Related works

Habil et al. [19] proposed automated clasification of colon histopathology images. They analyzed based on image patches in large dataset by utilizing Gabor filter banks. The classification were analyzed into 3 cases: normal vs. abnormal, cancer vs. non-cancer and four-class classification. Their proposed method achieved 80% of classification accracy approximately.

Rahmadwati et al. [20] presented computer-assisted classification in cervical cancers by utilizing histology images. Their analyzed based on nuclear characteristics. Gabor filter descriptors were investigated to extract texture of nuclei in dataset. For classification step, hybrid k-means clustering algorithm was utilized for distingushing normal and abnormal cells in histological cervical cancer tissue.

However, the parameters of Gabor filter bank depend on a database. The design of filter bank is done by setting parameters manually. Therefore, the insignificant filters for representing the data are included. It is necessary to find a relevant parameters and remove insignificant parameters. In color image, researchers have proposed feature selection techniques to remove irrelevant Gabor patterns such as Sequential Forward Selection (SFS), Sequential backward Selection (SBS), Mutual information [21] and Minimum Redundancy and Maximum Relevance (mRMR) [22]. These techniques could not apply directly to our framework in multispectral images. Therefore, our objective of utilizing optimization algorithm is to find relevant Gabor patterns which suitable for overall multispectral bands in term of improving classification accuracy. The algorithm can mainly take the advantage to reduce dimensionality of feature and speed up computational time.

In multispectral images, Qi et al. [23] classified breast cancer tissue microarrays as well as low-magnification. They utilized a bag-of-visual-word technique with texture descriptors. The experiment was performed by applying SVM classifier with radial basis function for each individual multispectral band. The bands that achieved higher classification rate than their transformed gray scale RGB were chosen as candidates in final decision. The majority voting strategy was applied for final classification result. In addition, they compared classification performance with conventional RGB images. Their experimental result showed multispectral images achieved higher classification rate than RGB images.

2.5 Multispectral bands selection

Band selection [24–28] is one of the popular techniques and widely used in remote sensing. This technique refers to select the optimal subset of multispectral bands. The advantage of band selection is removing redundancy of data and remove irrelevant spectral bands for improving analysis performance. In particular, the computational time of utilizing subsets of spectral bands is faster than dealing with whole multispectral bands. However, the aim of this study focuses on different point of view. This dissertation aims to analyze the significance of individual multispectral band in terms of characterizing cancer and non-cancer cell.

2.6 Computer aided diagnosis system

CAD systems in cancer diagnosis have been proposed in cervical cancer [29][30], breast cancer [23], and white blood cell [17] by utilizing multispectral images. Some publications analyzed cancers in multispectral images. Their result showed that multispectral images can enhance the system performance compared with the conventional color images. Wu et al. [29] and Xin et al. [23] studies have shown the possibility of multispectral imaging technologies in pathological analysis. Moreover, multispectral images also contribute to researchers to get more knowledge and new perspective on tissues and cells.

Irshad et al. [31] proposed computational method for mitosis detection in breast cancer histopathology in multispectral images. First, focal plane selection is performed based on maximum gradient information. They reduced multispectral bands by considering absorption spectra properties. Next, gray level co-occurrence matrix are investigated to extract feature descriptors in region of interest. Finally, classification performances are compared with four difference kinds of classifiers including decision tree, multilayer perceptron, linear support vector machine and non-linear support vector machine. Their proposed framework with multispectral histology images have beneficial to exploit the use of spectral and spatial information to see beyond the visualization of human.

2. Related works

Several studies have been proposed computer aided diagnosis system for detection and classification of thyroid follicular adenoma and thyroid follicular carcinoma in cytological images [32],[33],[34].

Gopinath et al. [32] developed an automated computer-aided diagnosis system for distinguishing benign and malignant of thyroid nodules from cytological images. In the first stage, nuclear segmentation was performed based on morphological operations and watershed transform algorithm. Next, segmented nuclei were extracted features including discrete wavelet transform, gray level co-occurrence matrix and Gabor filter banks. The k-nearest neighbor, Elman neural network and support vector machine are utilized to classify benign and malignant of thyroid. The experimental results showed by combining textural features from Gabor filter banks with Elman neural network achieved highest classification rate 93.33%.

Wang et al. [33] proposed detection and classification system for classifying thyroid follicular adenoma and thyroid follicular carcinoma in high magnification. They were analyzed based one nuclear characteristic by extracting several features and combined them together such as geometrical features, color features and textural features. Thus, each nuclei represented in high-dimensional feature vector. By utilizing support vector machine with radial basis function with kernel, the classification performance successfully achieved 100% based on leave-one-out cross validation strategy. However, they performed on small dataset around 10 patients. This proposed system may not confirm stability and consistency. It require to perform experiment in large amount of dataset.

Jung et al. [34] analyzed the impact of nuclear segmentation on classification of thyroid follicular lesions. Various kinds of nuclear segmentation algorithms are performed and compared the performance in classification step for classifying thyroid follicular adenoma and thyroid follicular carcinoma. The result showed that nuclear segmentation algorithm was importance for classifying thyroid follicular lesions.

Recently, deep neural networks algorithm is popular and was applied in various kinds of research field for classification. Due to deep neural network perform well in many applications of both research and practical. In medical image analysis, researcher have been developed computer aided diagnosis systems by

investigating deep neural networks for analysis in breast cancer [35],[36] and thyroid nodules [37]. Dan et al. [36] analyzed mitosis detection of breast cancer in histology images. Their system achieved promising results. Antonis et al. [37] proposed a multi-classifier diagnostic system for classifying benign and malignant of thyroid nodules in HE stained cytological images. Their experimental results showed that by combining several classifiers in k-nearest neighbor, probabilistic neural networks, bayesian and the majority voting strategy, the classification accuracy was outperformed single classifier in probabilistic neural networks. Deep neural networks algorithm was applied in many applications. However, it has some limitations for consideration. Deep neural networks acquire large number of training dataset, high computational resources and time consuming. An application which provide limitation of computational resources and important issue of the runtime, deep neural networks may not appropriate. Other classifiers may achieve similar or better results than deep neural networks.

For 3D medical image analysis, Ali et al. [38] proposed classification system of renal cell carcinoma tissue image from confocal laser scanning microscope. Their mainly focused on extracting efficient feature descriptors for grading cancer specifically in three-dimensional texture analysis methods. The result showed that utilizing Haar wavelets with principle component analysis achieved the highest classification rate 90%.

Chapter 3

System overview of proposed method

3.1 Introduction

This chapter explains details of the proposed system. It consists of two main parts including nuclei segmentation and nuclear characteristic analysis for cancer cells images. The proposed method in nuclear segmentation is based on pixel-based classification as described in section 3.2. Section 3.3 explain the overview of proposed method for nuclear characteristic analysis for cancer cells images. The proposed system will apply to analyze HCC and FTA as explain in chapter 4 and 5, respectively.

3.2 Nuclear segmentation

In subcellular structure, nuclei is one of the significant factor for cancer analysis in pathology images. Due to the morphological features and chromatin patterns change in cancer cells. That is the reason to utilize the properties of nuclei for distinguishing normal and cancer cells. Most of normal cells appear as a rounded or ellipsoid shape, and the sizes and morphological features of the nuclei tend to be uniform as shown in Fig. 3.1 . On the other hand, cancer nuclei have irregular shapes, variable in size and atypical chromatin patterns as shown in Fig. 3.2.

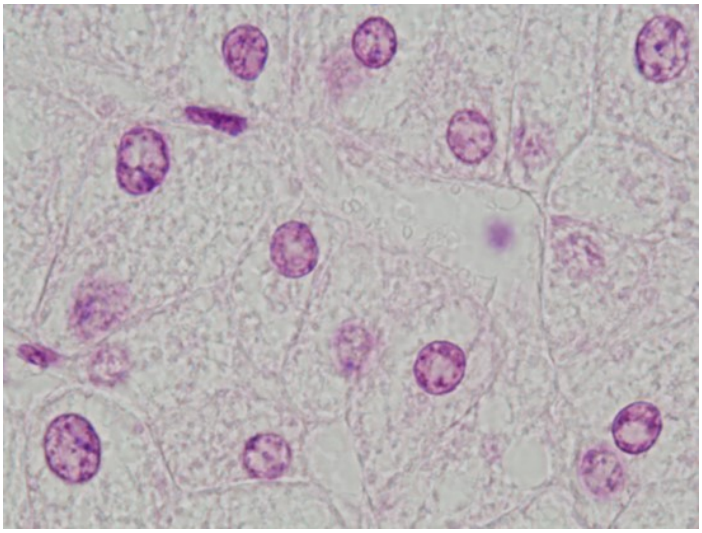

Figure 3.1: Normal liver tissue.

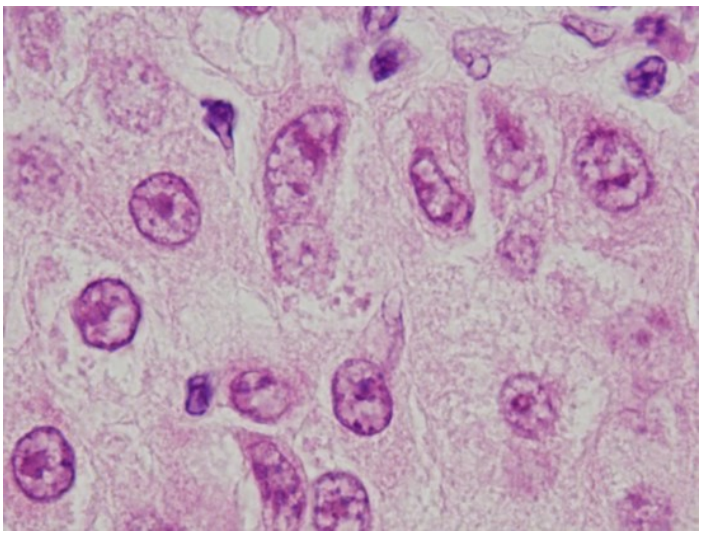

Figure 3.2: Hepatic cancer tissue.

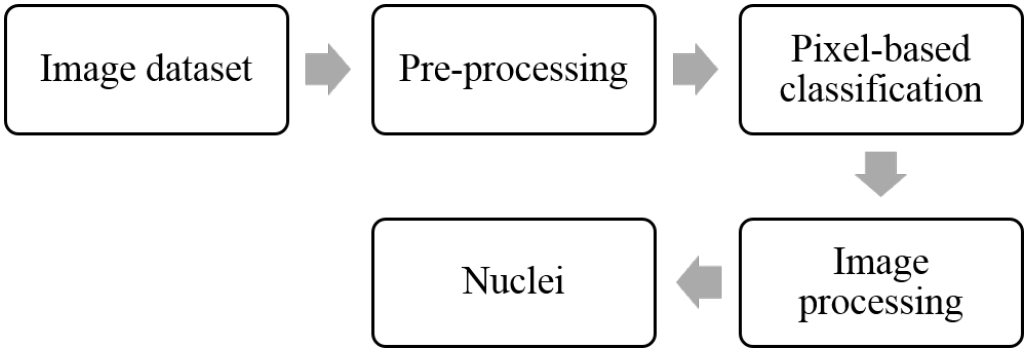

Figure 3.3: System overview of nuclear segmentation.

Figure 3.3 shows the overview of proposed system in nuclear segmentation. The system mainly contains three processes. In the first process, preprocessing techniques are applied in each image for improving image quality. Next, pixel-based classification method is investigated to classify each pixel. In the last process, we enhance images by using image processing techniques. Finally, we can get segmented nuclei and used these nuclei for classification in the next step.

3.2.1 Image preprocessing

Image preprocessing technique is the first step for processing data. The propose of this step is to improve the image quality from raw data. Due to image artifacts can be generated while capturing image from CCD camera and it effect on images. However, There are many preprocessing techniques to deal with different kinds of problems which depend on imaging technologies and capturing techniques. In this dissertation, we utilized multispectral images and 3D images to perform experiments for details of investigating image preprocessing will explain in chapter 4 for multispectral images and chapter 5 for volumetric data.

3.2.2 Pixel-based classification

Pixel-based classification technique is one of segmentation methods which investigate machine learning algorithms instead of image processing algorithms. Therefore, each pixel in images is classified into one subclass by using machine

learning algorithms. Pixel-based classification can be supervised learning or unsupervised learning. This dissertation perform experiments based on supervised learning in multispectral images and unsupervised learning in 3D images. The first step is to extract feature vector for representing each pixel. In the second step, these feature vectors are applied as input for training in random forest classifier for generating model of random forest. For testing, the result of random forest classifier give posterior probability of each class. The aim of this study is to segment nuclei. Thus,we are interested in posterior probability of nuclear class. The pixel is belong to nuclear area, if it has high probability in nuclear class.

3.2.2.1 Random forests

Random-forests algorithms has been used in wide variety of computer visions, such as digit recognition, keypoint recognition, visual word clustering, object segmentation, pose estimation, organ detection, and so on. It was proposed by Breiman [39]. Random forests classifier can solve a large variety of high dimensional problems with low computation time, high performance and high accuracy. Random-forests is an ensemble of several decision trees. Each tree is grown by using some types of randomization. The structure of each tree is binary decision tree which is created in a top-down manner as shown in Fig. 3.4.

In training procedure, Each tree is trained separately by choosing subset I' randomly in training data $I, I' \subseteq I$. At node n, learning proceed iteratively to split the training data I_n into left and right subsets I_l and I_r in accordance with a threshold t of some splitting function $f(v_i)$ of the feature vector v,

$$I_l = \{i \in I_n | f(v_i) < t\} \tag{3.1}$$

$$I_r = I_n \backslash I_l \tag{3.2}$$

At each split node, several candidates are generated randomly by using the splitting function f and threshold t. The one candidate that has a maximal

information gain about the corresponding node is chosen.

$$\Delta E = -\frac{|I_l|}{|I_n|}E(I_l) - \frac{|I_r|}{|I_n|}E(I_r) \tag{3.3}$$

According to eq. 3.3, ΔE is information gain calculated by entropy estimation, where $E(I)$ is the Shanon entropy of the classes in the set of training data I. The recursive training ended when the training process reaches maximum depth of the tree or until no further information gain is possible. Consequently, at every leaf node has a posterior probability and class distributions, $P(c|n)$ are estimated empirically as a histogram of the class labels c_i of the training examples, i, that reached node n.

In the testing step, feature vector is used as an input to the trained random forests. The final class distribution is generated by averaging the class distributions over the leaf nodes $L = (l_1, l_2, , l_t)$ reached for all T trees :

$$P(c_i|L) = \frac{1}{T}\sum_{t=1}^{T} P(c_i|l_t) \tag{3.4}$$

In eq. 3.4, T is the number of trees and c_i is a final class of an input feature if and only if $P(c_i|L)$ has the maximum posterior probability.

3.2.3 Image enhancement

Since we performed nuclear segmentation based on pixel-based classification, the result is not give perfect segmentation. It is important to apply image processing techniques in order to reduce the noise in image and non-nuclei area. The objective of this step is improve quality and remove noise of images for extracting nuclei effectively. Firstly, the connected component are investigated to measure the size of each object in image. If the size is smaller than threshold value, that area will be removed. The removed area can be non-nuclei area or lymphocyte area. Next, morphological operators are utilized to remove noise and refine the shape of nuclei area. Finally, we obtain segmented nuclei. These segmented nuclei are used to analyze cancer in the next step which is classification. The details of classification describe in section 3.3.

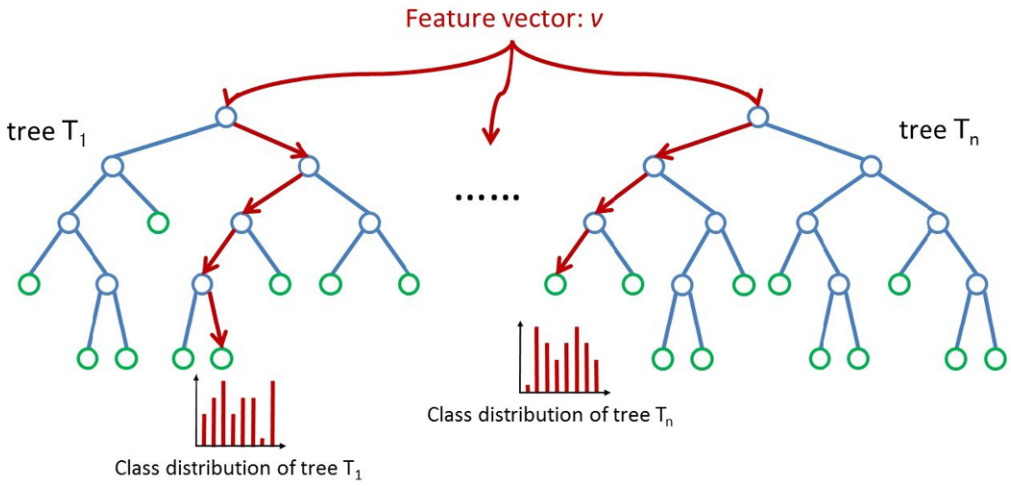

Figure 3.4: Structure of random forests.

3.2.3.1 Morphological operator

Morphological operator is based on a set theory that represents shapes [40]. In term of image, elements of a set are pixels in an image. Morphological methods are widely used in image processing, which in the field of noise reduction, segmentation, restoration, enhancement, shape analysis, etc. The basic morphological operators are erosion and dilation which implicate an image A and a structure element E. The structure element E is constructed in 2D Euclidean space ε^2.

Dilation of image A by S is given by

$$A \oplus E = \left\{ x \in \varepsilon^2 | x = a + e, for a \in A, e \in E \right\} \tag{3.1}$$

Erosion of the image A by S is given by

$$A \ominus E = \left\{ x \in \varepsilon^2 | \forall e \in E, \exists a \in A such that x = a - e \right\} \tag{3.2}$$

The closing and opening operators are derived from erosion and dilation, are defined by

Closing:

$$A \bullet E = (A \oplus E) \ominus E \tag{3.3}$$

Opening:

$$A \circ E = (A \ominus E) \oplus E \tag{3.4}$$

In case of noise reduction, morphological operator reduces the noise based on shape characteristics of the input image, which is characterized by the structuring element.

3.3 Nuclear characteristic analysis for cancer cells images

In this section, we explain classification step which investigate in this research. It mainly consist of feature extraction, classification model as describe in section 3.3.1 and 3.3.2, respectively. As the result of nuclei segmentation in section 3.2, the segmented nuclei were applied in classification step for cancer analysis by extracting statistical and textural feature for representing nuclear characteristics. Next, classification model and evaluation strategies were investigated for final decision.

Figure 3.5 shows the overview of proposed system in cancer classification based on nuclear characteristics. First step is to extract feature for each segmented nuclei. Next, bag-of-visual-word (BoW) model is utilized to reduce the dimension of feature vector and seek relevant feature descriptors for representing nuclear characteristic significantly. Random forests classifier is performed to classify normal and cancer cells nuclei. Lastly, majority voting strategy are applied to make the final decision.

3.3.1 Feature extraction

The feature is defined as a set of measurements which describe the property of an object and compute significant characteristics of the object through numerical representation. Features can be categorized into low-level features and high-level

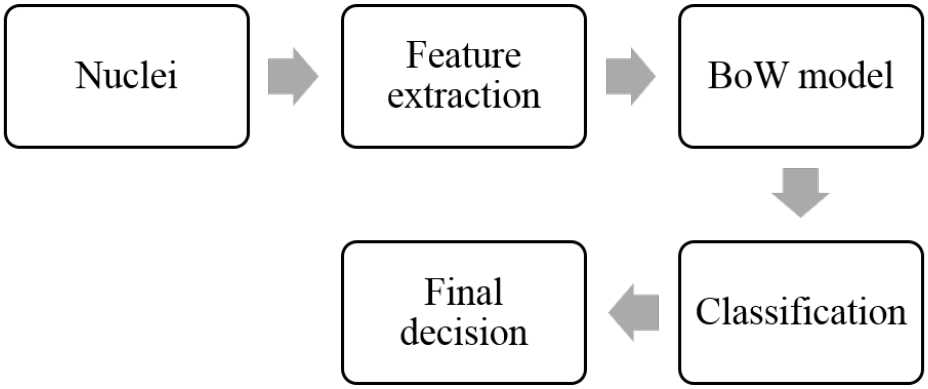

Figure 3.5: System overview of classification model.

features. Low-level features compute directly from original images whereas high-level features extract based on low-level features. Feature extraction is investigated in the field of pattern recognition and image processing. Feature extraction is a process to transform the input data into a set of features. It mainly contain information related to texture, shape or color intensity. The beneficial of feature extraction is to reduce dimension of data, remove redundancy and extract relevant information from input data. Feature extraction have to be done before performing classification of objects. If we can find suitable feature extraction techniques to represent objects in dataset, we can improve classification accuracy when utilized feature descriptors to classify objects in classification step.

In the study of HCC classification in multispectral images as describe in chapter 4, Gabor descriptors are used to represent chromatin pattern inside nuclei. In addition, we proposed optimization of Gabor parameters in order to select significant parameters which suitable for all multispectral bands and improving classification accuracy. Thus, This section also explain basic concept of Gabor filter banks. In chapter 5, we classify subclassification of follicular thyroid adenoma in favor benign and borderline types by utilizing 3D images. In this study, 3D feature descriptors are investigated to extract information of nuclei in 3D images. Specifically, this section also explain basic concept of 3D feature descriptors especially in 3D gray level co-occurrence matric (GLCM).

3.3.1.1 Gabor filter

In this study, we investigated Gabor descriptors. Gabor filtering is one of the textural feature extraction techniques, and widely applied in various kinds of recognition applications including medical image diagnosis system [41]. Due to Gabor descriptors extract the significant texture characteristics of the specific region of interest.

The 2D-Gabor filters explained in [42] can be defined as

$$\begin{aligned} g_{uv\theta}(x,y) &= \exp(-\tfrac{x'^2+\gamma^2 y'^2}{2u^2})cos(2\pi\tfrac{x'}{v}+\psi), \\ x' &= x\cos(\theta)+y\sin(\theta), \\ y' &= y\cos(\theta)-x\sin(\theta) \end{aligned} \tag{3.5}$$

where $g_{uv\theta}$ denotes a Gabor filter with spatial aspect ratio γ, standard deviation of Gaussian u, phase offset ψ and orientation θ. x, y are spatial coordinates. v is the wavelength and $1/v$ is spatial frequency of the cosine factor. The ratio u/v determines the spatial frequency bandwidth bw. The relationship between the half-respond of spatial frequency bandwidth bw and the ratio u/v can be expressed as

$$bw = \log_2 \frac{\frac{u}{v}\pi + \sqrt{\frac{\ln 2}{2}}}{\frac{u}{v}\pi - \sqrt{\frac{\ln 2}{2}}}, \frac{u}{v} = \frac{1}{\pi}\sqrt{\frac{\ln 2}{2}}\frac{2^{bw}+1}{2^{bw}-1} \tag{3.6}$$

The image features can be extracted by convolution of original image $I(x, y)$ with a set of Gabor patterns as described

$$G_{uv\theta}(x,y) = I(x,y) * g_{uv\theta}(x,y) \tag{3.7}$$

where $G_{uv\theta}(x, y)$ represents the convolution result corresponding to the original image and Gabor filter $g_{uv\theta}$.

Gabor feature descriptors may provide meaningful information from region of interest. The main key of generating Gabor filter bank is scales and orientation parameters. In particular, the combination of their parameters will produce different classification results. Therefore, this study focuses on orientation θ and

spatial frequency bandwidth bw parameters for creating a set of Gabor filters and other parameters are fixed.

3.3.1.2 Gray level co-occurrence matrix (GLCM)

For computation of 3D GLCM in three-dimensional image [43], [44], a co-occurrence matrix is a n x n matrix, where n is the number of gray levels in a given image. Basic concept of the computation is similar to a conventional 2D GLCM. A co-occurrence matrix collects the number of differences in intensities of two pixels indexed i and j in specific directions and distances. The co-occurrence matrix represents a displacement as $d = (dx, dy, dz)$ where dx, dy and dz denote the number of pixel moved along x, y and z axis, respectively in volumetric data, respectively. 3D GLCM can be defined as

$$p(i,j) = \sum_{z=1}^{B_z-d_z} \sum_{y=1}^{B_y-d_y} \sum_{x=1}^{B_x-d_x} \begin{cases} 1 & if G(x,y,z) = i \wedge G(x+d_x, y+d_y, z+d_z) = j \\ 0 & otherwise \end{cases} \tag{3.8}$$

where 3D GLCM elements $p(i,j)$ compute within moving box B. Furthermore, displacement vectors contain 13-directions with offset D as shown in Table 3.1. Actually, direction 1, 2, 3, and 4 are commonly used in 2D GLCM, and the additional nine directions are investigated in 3D GLCM. Next, haralick features [45, 46] is computed from the co-occurrence matrix to describe the texture of images. This study considers 12 statistical measurements as shown in Table 3.2 including Energy, Entropy, Correlation, Contrast, Variance, Sum Mean, Inertia, Cluster Shade, Cluster Tendency, Homogeneity, Max Probability, and Inverse Variance.

3.3.2 Classification model

3.3.2.1 Bag of Words model

Bag of Words model (BoW) approaches have been investigated in various kinds of computer vision applications as one of the powerful techniques. The main process of BoW model is to transform a set of high-dimensional local features into a single feature vector for representing region of interest. This representation has

Table 3.1: Displacement vectors for co-occurrence matrix generation.

ID	Displacement vector	Direction (horizontal, vertical)
1	$(0, D, 0)$	$(0°, 0°)$
2	$(-D, D, 0)$	$(45°, 0°)$
3	$(-D, 0, 0)$	$(90°, 0°)$
4	$(-D, -D, 0)$	$(135°, 0°)$
5	$(0, D, -D)$	$(0°, 45°)$
6	$(0, 0, -D)$	$(none, 90°)$
7	$(0, -D, -D)$	$(0°, 135°)$
8	$(-D, 0, -D)$	$(90°, 45°)$
9	$(D, 0, -D)$	$(90°, 135°)$
10	$(-D, D, -D)$	$(45°, 45°)$
11	$(D, -D, -D)$	$(45°, 135°)$
12	$(-D, -D, -D)$	$(135°, 45°)$
13	$(D, D, -D)$	$(135°, 135°)$

Table 3.2: statistical measurements of haralick descriptors.

ID	Statistical measurement	Equation
1	Energy	$\sum_i \sum_j p(i,j)^2$
2	Entropy	$-\sum_i \sum_j p(i,j) log(p(i,j))$
3	Correlation	$\frac{\sum_i \sum_j (i,j) p(i,j) - \mu_x \mu_y}{\sigma_x \sigma_y}$
4	Contrast	$\sum_{n=0}^{N_g - 1} n^2 \{\sum_{i=1}^{N_g} \sum_{j=1}^{N_g} p(i,j)\}, \lvert i-j \rvert = n$
5	Variance	$\sum_i \sum_j (i-\mu)^2 p(i,j)$
6	Sum Mean	$\sum_{i=2}^{2N_g} i p_{x+y}(i,j)$
7	Inertia	$\sum_i \sum_j (i-j)^2) p(i,j)$
8	Cluster Shade	$\sum_i \sum_j ((i-\mu_i) + (j-\mu_j)^3 p(i,j)$
9	Cluster Tendency	$\sum_{i=1}^{N_g} \sum_{j=1}^{N_g} (i+j-2\mu)^k p(i,j)$
10	Homogeneity	$\sum_{i=1}^{N_g} \sum_{j=1}^{N_g} \frac{p(i,j)}{1+\lvert i-j \rvert}$
11	Max Probability	$max_{i,j} p(i,j)$
12	Inverse Variance	$\sum_i \sum_j \frac{1}{1+(i+j)^2} p(i,j)$

shown the effectiveness in image classification and categorization. Specifically, BoW model has been successfully applied in medical image analysis and achieved high performance especially in histopathology images. In histopathology image analysis, textural features are mainly extracted in nuclear region. Then, k-means algorithm is computed to generate dictionary. As a result, each cluster center represents a feature vector of its class, called visual word. Consequently, each pixel in region of interest finds the nearest visual word index and form histogram frequencies. The histogram is a novel representative of interested region.

3.3.2.2 Texture classification model

In this dissertation, the classification is based on BoW model of textural features by extracting from nuclear region. Figure 3.6 shows the overview of classification procedures step by step. Firstly, nuclear texture is extracted utilizing textural feature descriptors. Then, BoW model is applied to represent nuclei as a histogram frequency. The histogram of visual words provides a discriminative characteristic for each nucleus. A random forest classifier [39] is adopted in classification step. The histogram is investigated as an input for generating model of random forest in training step and also used in testing step. The posterior probability of each class is obtained as a result of random forest classifier. The class that has maximum posterior probability, is selected as the final class of that nucleus. Finally, majority voting strategy is utilized for making a final decision in patient level. Let q_c be the total number of nuclei which belong to class c and r be total number of nuclei. Also let the probability of a patient classified into class c be $p_c = q_c/r$. Given a threshold T, if maximum of p_c is greater than T, then the patient is classified into class c.

3.4 Evaluation strategies

3.4.1 k-fold cross validation

Normally, classification systems have two steps.

i. Training: The classifier learns from training data to generate the model.

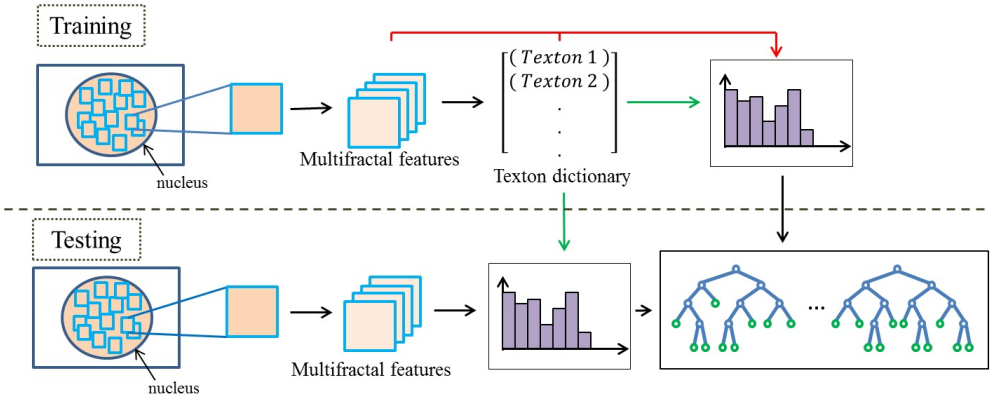

Figure 3.6: Schematic for construction of textons based classifier using Gabor descriptors. In the training step, the gabor features are extracted for each nucleus. Then, the features are clustered via k-means to identify the cluster centroids as texton. The feature space is reduced to the index of the nearest texton. After that, the bag of textons forming the histogram model for each patch. In the final step, random forests classifier performed by using the histogram as an input to generate several decision trees. Classification of a new nucleus involves first constructing the corresponding texton signature and then using model of random forests to classify normal and cancer.

ii. Testing: The classifier predicts the system performance.

In order to reduce the bias from classification techniques, validation strategies is necessary to apply. The k-fold cross validation is one of validated method and widely used for evaluation. In the first step, dataset are divided randomly into k disjoint subsets of approximately equal sizes. Next, $k-1$ subsets are utilized to train the classifier and another subset is for testing. The process iteratively perform for all disjoint k subsets to estimate the clssifier.

3.4.2 Classification rate(CR)

The percentage of classification rate is defined as follow,

$$CR = \frac{\sum_{i=1}^{K} n_i}{N} \times 100 \tag{3.9}$$

where n_i is the total number of correctly classified to the i^{th} class, M is the number of class, and the total number of samples data (N).

Moreover, The final classification accuracy of applying k-fold cross validation is the average of classification rate (avgCR) as follow.

$$avgCR = \frac{\sum_{i=1}^{k} CR}{k} \tag{3.10}$$

Where k is number of fold in k-fold cross validation.

3.4.3 Statistical measures

In binary classification, the classifier performance is computed through various statistical measurement including precision and recall especially in pattern recognition and information retrieval fields. The measurement is performed by analyzing the result from classifier. The computation of precision and recall are defined as follows.

$$Precision = \frac{TP}{TP + FP} \tag{3.11}$$

$$Recall = \frac{TP}{TP + FN} \tag{3.12}$$

Chapter 4

Hepatocellular carcinoma classification in multispectral histopathology images

4.1 Introduction

Hepatocellular carcinoma is the second most of major death in worldwide especially men [4]. Specifically, hepatocellular carcinoma is a major cause of death in developing countries including Asia and Africa. Histopathology is a microscopic study of tissue especially in cancer diagnosis. Since the nuclei structure has a significant interpretation for cancer analysis in histopathological microscipic images. Figure 4.1 and 4.2 shows the multispectral sample images of HE-stained biopsy specimen in normal and HCC, respectively. The different characteristics of liver cell nuclei between normal and HCC are chromatin patterns and morphological properties. Therefore, the texture properties of nuclei are utilized to classify normal and HCC.

In this study, we analyze hepatocellular carcinoma in 100x magnification in order to clearly see chromatin pattern inside nuclei. The multispectral images are utilized for this study with aim to extend new technologies to explore an additional information beyond spatial and spectral information. This study proposes a classification approach of hepatocellular carcinoma (HCC) for classifying cancer and normal cells. Nuclear segmentation perform in the first step based

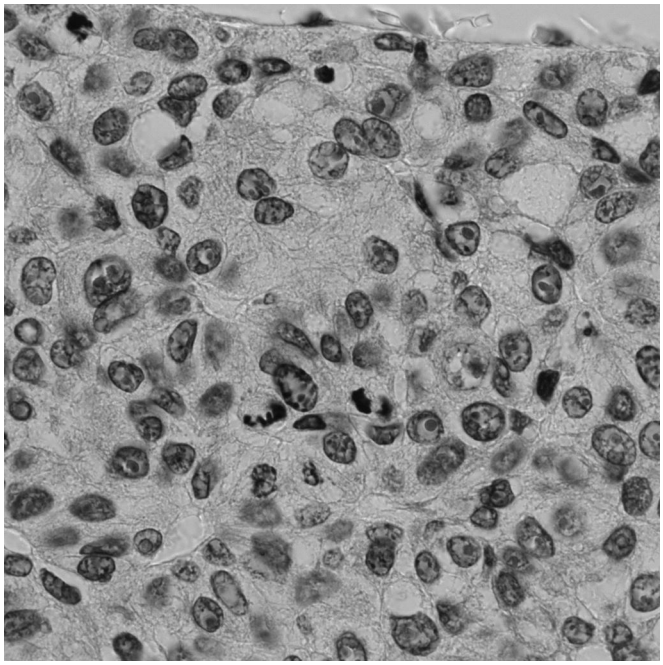

Figure 4.1: The 10^{th} band of normal liver histological image.

on supervised learning in pixel-based classification technique. In classification step, we extract features from Gabor filter banks. Moreover, we proposed an optimization algorithm to select relevant features. Then, Bag-of-visual-word with random forests classifier is employed to classify normal and cancer cells nuclei in hepatocellular carcinoma.

4.2 Image acquisition

The multispectral microscopic-camera created by Akasaka National Vision Research Center, Japan is investigated to capture multispectral dataset in this study. The camera system contains a 16-band rotating filter wheel with a 2048x2048 pixels per image using CCD camera. The wavelength range is in the visible spectrum from 400 nm to 750 nm. a multispectral image illustrate in gray scale image. At one position, multispectral microscopic-camera capture 16-band by changing the different narrow band of wavelength. Figure. 4.3 shows the example of HCC multispectral images of 16 spectral bands in our dataset. Figure 4.4 shows multispectral information which compose of 2D-spatial data along x and y directions

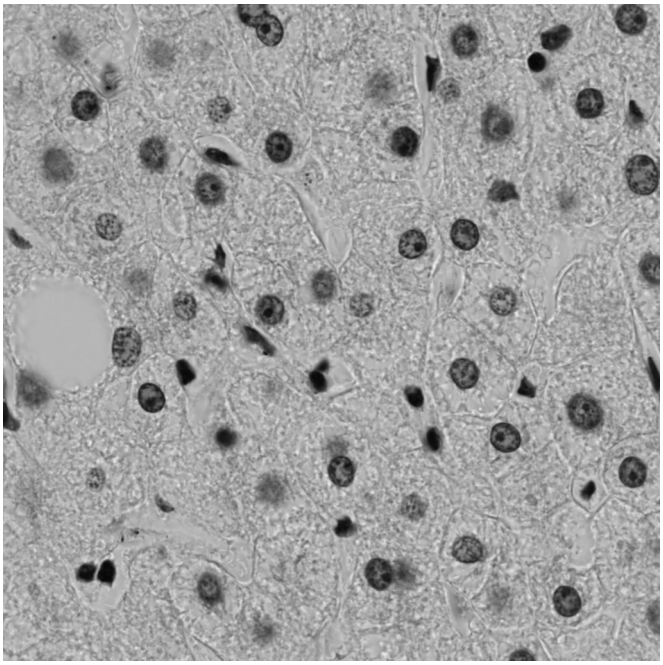

Figure 4.2: The 10^{th} band of HCC histological image.

and 1D-spectral wavelength information in λ dimension. It can be formed as an image cube from spatial and spectral information. At the same position of 16 bands, the intensity value of spatial coordinates along wavelength dimension is called spectrum. In addition, the spectrum indicate a particular properties of its spatial point.

Our dataset obtained from US Biomax, Inc., (Rockville, MD, USA) and contained normal liver and HCC tissue microarray specimen. All tissue samples were verified with informed consent from patients. This study perform experiment with 19 patients of HE stained histopathology liver tissues including normal and HCC multispectral images. Experienced pathologists distinguished a set of multispectral images as normal or cancer. In order to clearly see chromatin patterns in each nucleus, the multispectral dataset captured at 100x magnification with no overlapping area and obtained 162 images. One data sample have 16 multispectral bands.

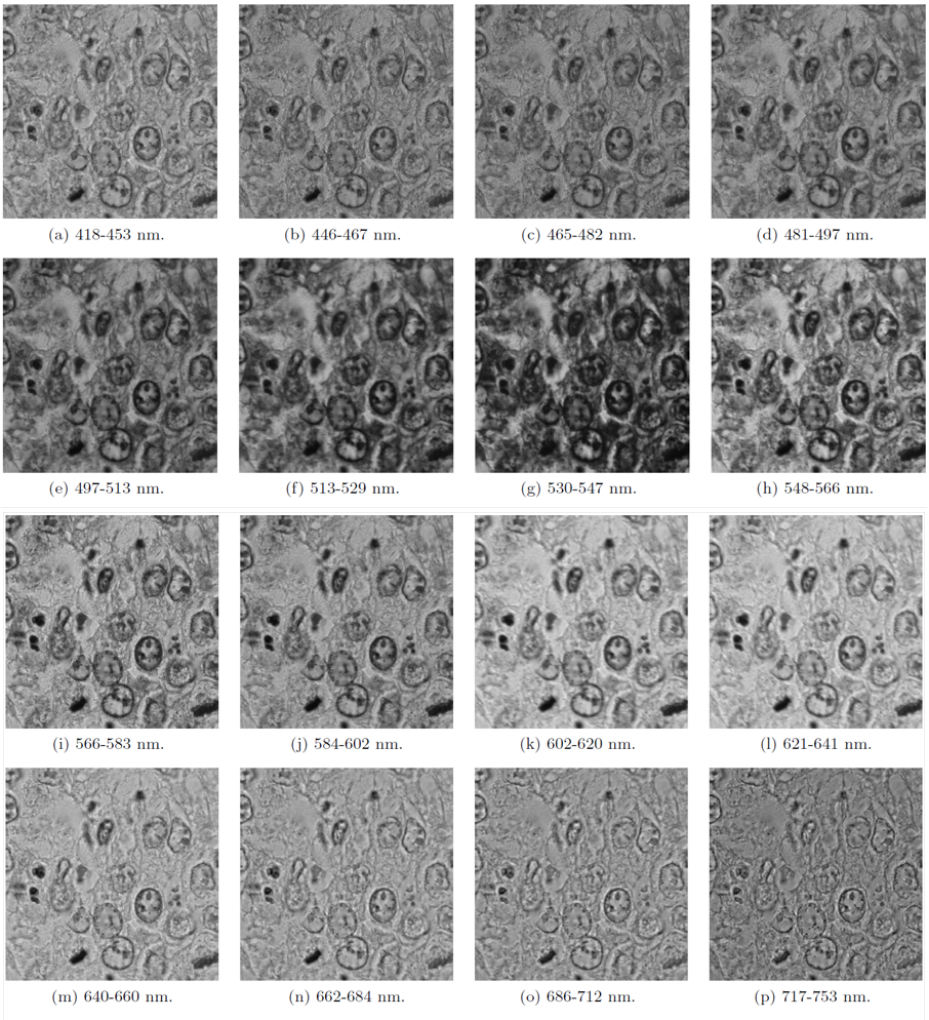

Figure 4.3: HE stained histopathology images captured from different wavelength intervals. (a) to (p) represent multispectral bands from the 1^{st} to 16^{th} band, respectively.

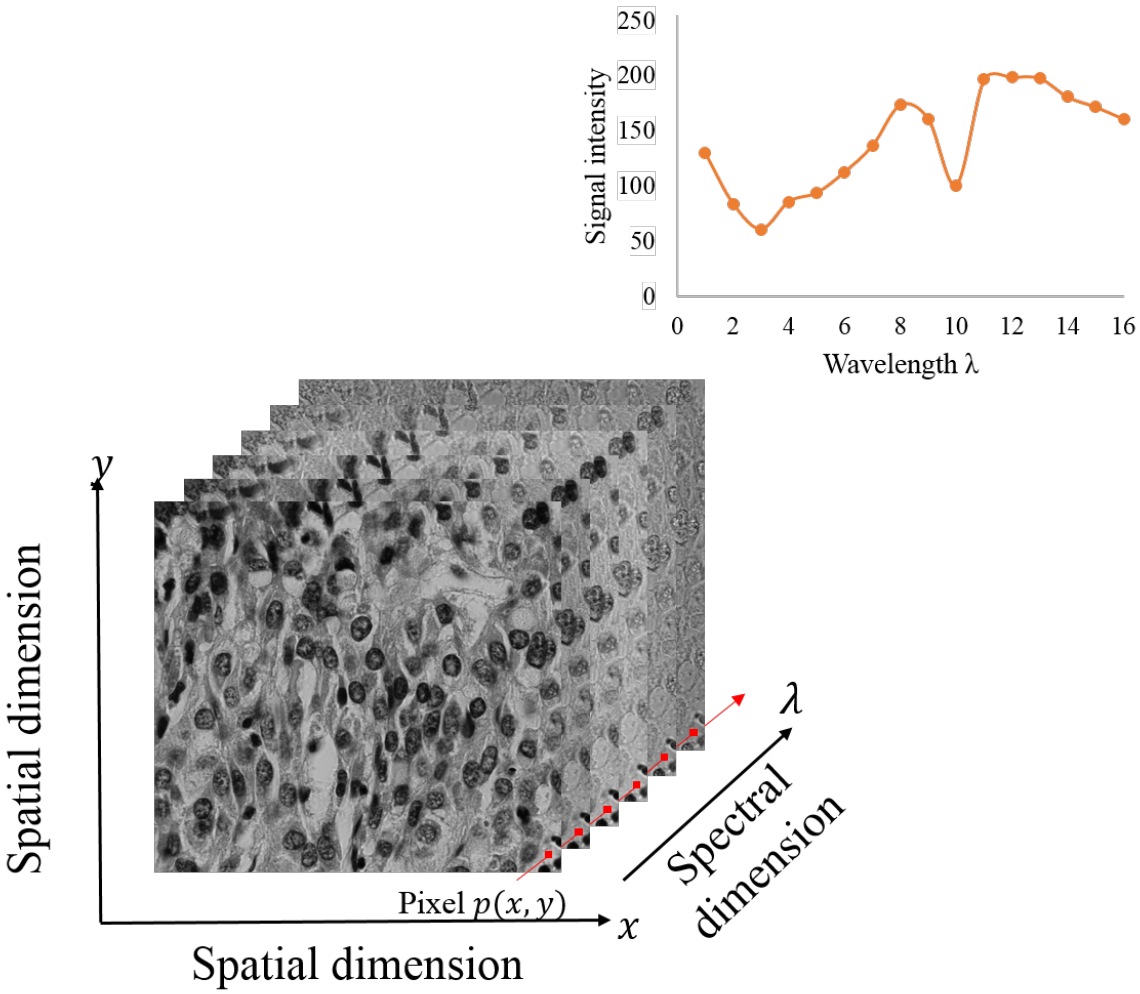

Figure 4.4: Image acquisition, Multispectral image cube acquired 2D-spatial information in x, y direction and 1D-spatial information along λ direction. At pixel $p(x, y)$, spectrum is constructed by plotting the signal intensity versus wavelength.

4.3 Image preprocessing of multispectral images

The light microscope was employed to capture multispectral image. In the first step, a CCD exposure time and light intensity were set before taking images. Then, multispectral images were taken under the same condition in order to compute the performance of data. However, some factors of image artifact can be happen such as non-uniform illumination during capturing the multispectral image. This problem affect image quality. In this study, image preprocessing technique is utilized to remove the artifacts. It acquired an additional reference image $B(x, y; \lambda_j)$ under exactly the same acquisition condition in a blank area of the tissue slide, where x and y are spatial coordinates of the image and λ_j is wavelength interval of j^{th} band. Therefore, normalized data $I(x, y; \lambda_j)$ can be described as

$$I(x, y; \lambda_j) = \frac{S(x, y; \lambda_j)}{B(x, y; \lambda_j)} \tag{4.1}$$

where $S(x, y; \lambda_j)$ and $B(x, y; \lambda_j)$ are an original image and no cell component slide image in multispectral data respectively. Figure. 4.3 shows the example of multispectral dataset after applying pre-processing technique for all 16 bands.

4.4 2D nuclei segmentation

The cell components mainly contain four types in our dataset including nuclei, cytoplasm, lymphocyte and blank regions. The propose of segmentation is to extract nuclear regions in normal liver and HCC images. The segmentation method perform multi-class segmentation based on pixel-based classification and image processing technique. Even though, only nuclear region is considered to investigate for cancer classification. In order to get more precise and accurate segmentation, we apply multi-regions segmentation. The proposed method is based on supervise learning. Thus, annotation os 15 sample images are obtained by experts'. The content of annotation consist of four regions: nucleus, cytoplasm, lymphocyte and background regions for each sample image. Since nuclear and lymphocyte features are sometimes overlapped. Thus, nuclear and lymphocyte

class are combined and represented as one class. This experiment investigated 147 multispectral images with 19 patients.

From eq. 4.1, we have a multispectral image $I(x, y; \lambda_j), j = 1, ..., 16$. The spectrum at a point (x, y) along λ direction can be defined as a vector $V(x, y)$

$$V(x, y) = \{I(x, y; \lambda_1), I(x, y; \lambda_2), ..., I(x, y; \lambda_{16})\} \tag{4.2}$$

The spectrum given by equation (4.2) represents a pixel feature vector with 16 dimension. The pixel based-classification with randomforest classifier is investigated for distinguishing three cell components. In the training step, the input for generated random forest model are features vector and its label in annotated region. When we applied test data in random forest model, the prediction probability of each class is obtained. However, our objective is to segment nuclei. Therefore, only prediction probability of nucleus-lymphocyte class are considered. Consequently, these probabilities are normalized into gray scale image as shown in Fig 4.5(b).

Consequently, image processing technique is applied to improve the segmented result from pixel-based classification. Firstly, morphological opening operator and Otsu's binarization algorithm [47] were utilized to enhance gray scale image and convert to black and white image, respectively. Then, we removed small regions by applying morphological closing operator. However, lymphocyte still appeared in image. In fact, the size of lymphocyte is smaller than nucleus. Thus, we removed lymphocyte region by setting the threshold value. Figure 4.5(c) shows the result of investigating image processing technique. Lastly, the final result of segmented nuclei were detected Fig. 4.5(d). Our method mainly detected only focused nuclei which have clear boundary and focus. For out-of-focus nuclei, the probability of nuclear-lymphocyte class in that area is not high. the reason ia that the spectrum is more similar to other classes. Furthermore, when we applied image processing technique, the out-of-focus nuclei are removed. Our propose is to diagnose cancer from chromatin patterns in nuclei. Therefore, only focused nuclei are our target in this experiment.

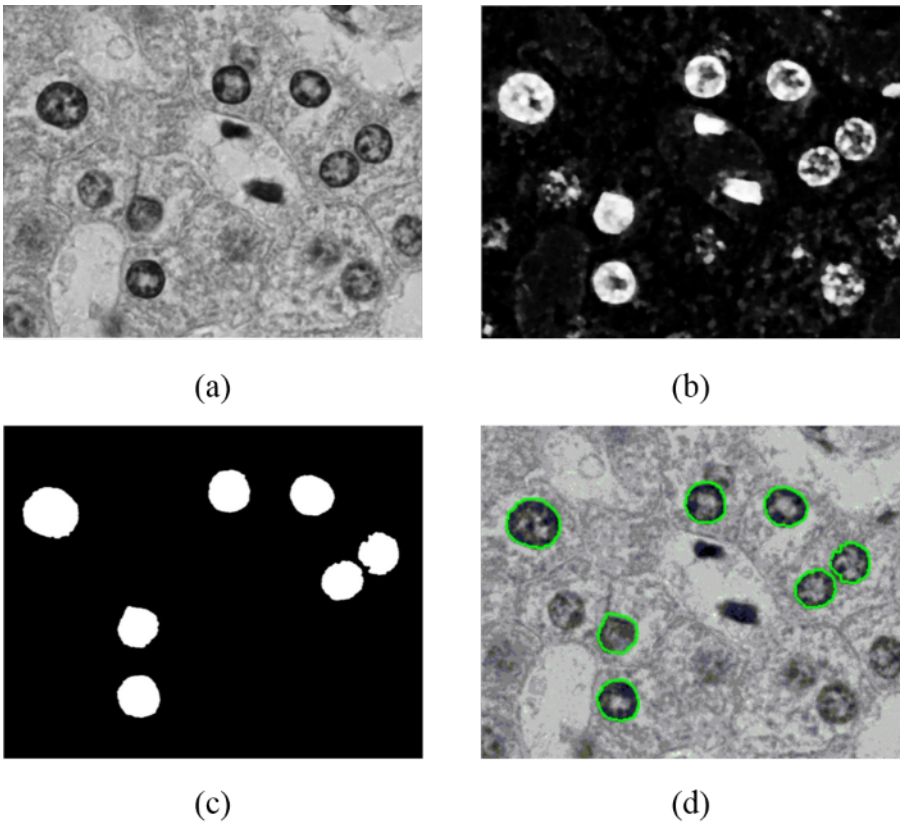

Figure 4.5: Step-bystep process of nuclei segmentation. (a) An example of original image in band 8^{th}. (b) Prediction probability of nuclei and lymphocyte class as normalized into gray scale image. (c) Final result by applying morphological operators. (d) The boundary of nuclei were detected.

4.5 Optimization algorithm for gabor parameters

In feature extraction step, the parameter setup for generating filter banks is also important to extract nuclear texture. Since a result of feature extraction directly influences classification performance. This study utilizes Gabor filters by considering parameter of frequencies and orientations. However, by manually setting, frequencies and orientations may not achieve high performance in liver cancer classification. We propose a concept to select subset of relevant Gabor parameters. The idea takes an advantage of improving the overall computational complexity. The objective of our proposed algorithm is to search the most effective parameter which is appropriate to overall multispectral bands. Moreover, this optimization technique also makes the data comparable under the same condition. In this study, the proposed optimization algorithm focused on selecting a subset of relevant parameters in Gabor filter, that is, orientation and spatial frequency bandwidth. The overview of proposed algorithm is shown in the optimization part of Fig. 4.8.

The algorithm is described as follows.

Given a data set of nuclei $D \subset \mathbb{Z}^{N\times 16}$, where N denotes the total number of nuclei in the multispectral database, we randomly select K, $(K < N)$ data from D for optimizing Gabor parameters. A and B denote a set of orientations and spatial frequency bandwidths of Gabor filter bank repectively, where $A = \{a_1, a_2, ..., a_m\}$ and $B = \{b_1, b_2, ..., b_s\}$. The optimal values in A and B are selected from the minimum ranking of mean square error (MSE) in texture classification model.

The proposed parameter optimization procedure is described in Algorithms 4.6 and 4.7. The Algorithm 4.6 is aimed to find the optimal subset of parameters A and B. Firstly, MSE of each parameter in A (MSE_A) and B (MSE_B) is computed in Algorithm 4.7. After that, first n-rank and p-rank of descending order of MSE_A and MSE_B respectively are selected as optimal values in A $(optA)$ and B $(optB)$. n and p are the number of selected elements in A and B respectively. The MSE_A is calculated using Algorithm 4.7 with input d, A, B. Secondly, the MSE_B is also computed from Algorithm 4.7 with input d, B, A. The optimization of Gabor parameters is described in Algorithm 4.7. The input

Algorithm 1

INPUT: data $d \subset \mathbb{Z}^{K\times 16}$, set of parameters A and B, and n and p are numbers of optimized A and B respectively
OUTPUT: $optA$ and $optB$

MSE_A= $OptimizedGaborParameter(d, A, B)$
MSE_B= $OptimizedGaborParameter(d, B, A)$
$optA$= first n-value of $SortDescent(MSE_A)$
$optB$= first p-value of $SortDescent(MSE_B)$

Figure 4.6: Algorithm 1.

consists of data d and parameter sets A and B. Firstly, a set of Gabor pattern f is generated by utilizing element of a_i with a set of B. Then, Gabor descriptors in each multispectral bands is calculated by taking convolution between original image I_j at band j and f. The error classification rate e_j is computed at band j from texture classification model as described in section 3.3.2.2. We iteratively compute e_j for every multispectral band. Thus, we calculate MSE of a_i, where $\mu = \frac{1}{16}\sum_{j=1}^{16} e_j$. Consequently, we iteratively change $a_i, i = 1, 2, ..., m$. Finally, the result of Algorithm 4.7 return MSE_A. Moreover, the MSE_B is also computed in Algorithm 4.7 as described above.

4.6 Experimental and results

4.6.1 Implementation

In classification step, segmented nuclei as a result from nuclear segmentation method were investigated to discriminate cancer and non-cancer cells. This experiment utilized Gabor descriptors to extract textural patterns in each nucleus. In this study, we generate parameters with a set of different frequencies and orientations and fix spatial aspect ratio and wavelength. We set $\theta = \{0°, 30°, 45°, 60°, 90°, 135°\}$ in orientation, the spatial frequency bandwidth $bw = \{0.6, 0.7, 0.8, 0.9, 1\}$, spatial aspect ratio $\gamma = 0.6$ and wavelength $v = 2$. Thus, we

Algorithm 2 OptimizedGaborParameter(d, A, B)

INPUT: data $d \subset \mathbb{Z}^{K\times 16}$, set of parameters A and B
OUTPUT: MSE_A

```
for i = 1 : m do
    a(i) = {a(i)|i = 1, ..., m}
    for j = 1 : 16 do
        F_j ← I_j * f(a(i), B)
        e_j ← Classify(F_j)
    end for
    MSE_a(i) = (1/16) Σ_{j=1}^{16} (e_j − μ)^2
end for
MSE_A = {MSE_a(i)|i = 1, ..., m}
return MSE_A
```

Figure 4.7: Algorithm 2.

obtain 30-Gabor patterns. Moreover, optimization of Gabor parameter is performed on our proposed algorithm. Due to a set of Gabor patterns may contain irrelevant patterns and it may affect the classification accuracy. In this experiment, we randomly get 25% of nuclear database to find relevant parameters which are suitable for all multispectral bands. The first three ranks of values in parameter θ and bw are selected as a result from Algorithms 4.6 and 4.7. Thus, we obtain 9-Gabor patterns. After extracting feature descriptors, classification procedure is performed for each individual multispectral band as shown in Fig. 4.8. Our experiment created 30 visual vocabularies of dictionary. This number of visual words provides the optimal classification rate. The final decision is specified by majority voting strategy in patient level. Furthermore, k-fold cross validation (CV) is applied for evaluating the performance. The classification accuracy obtain from the average accuracy over k-fold. Specifically, we compared the classification performance by utilizing all Gabor parameters and optimized Gabor parameters in this study. Figure. 4.8 shows the overview of classification

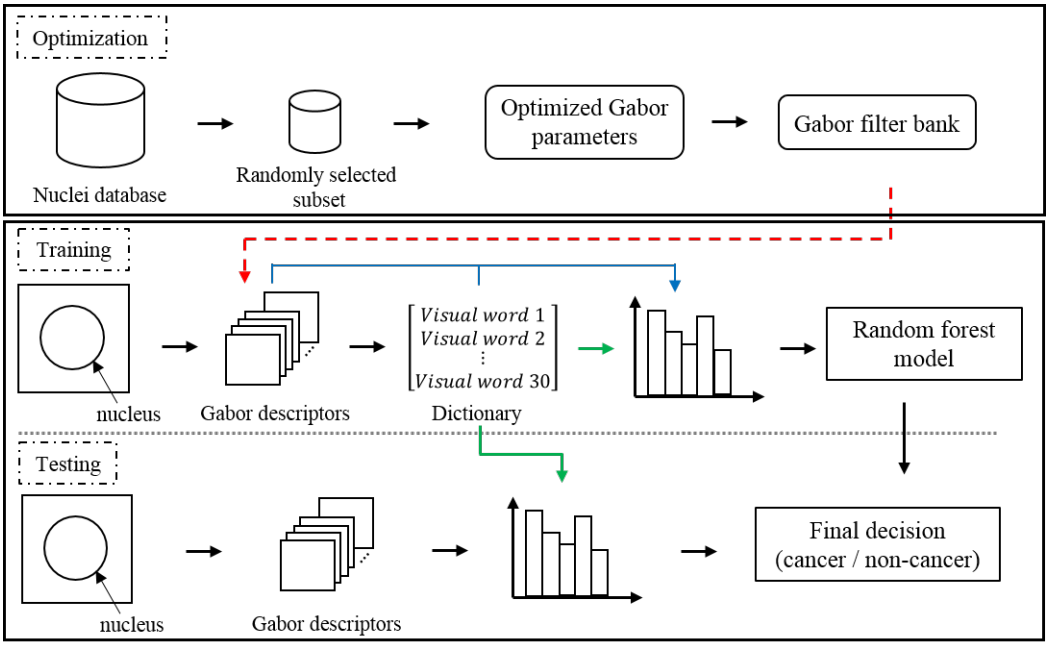

Figure 4.8: Schematic for filter-bank construction and BoW based classifier using Gabor descriptors. In the training step, the Gabor features are extracted for each nucleus using Gabor filter bank from the result of optimization algorithm. Then, the features are clustered via k-means to identify the cluster centroids as visual words. The feature space is mapped to the index of the nearest visual word. After that, the bag of visual words forming the histogram model for each nucleus. In the final step, random forests classifier performed by using the histogram as an input to generate decision trees. Classification of a new nucleus involves first constructing the corresponding visual word signature and then using model of random forests to classify normal and cancer cell.

procedures which mainly contain three steps: optimization, training and testing.

In addition, we performed experiment by combining the multispectral bands into several color spectrum according to the reference of wavelength interval of each color spectrum as shown in Table 4.2. The classification was performed by concatenating the histogram of visual words in each band. Consequently, random forest classifier and majority voting strategy were performed for final decision.

4.6.2 Parameter selection

The result after performing optimization of Gabor parameters is the first three ranks of a subset in parameter θ and bw. In this experiment, the relevant param-

eter in $\theta = \{0°, 30°, 60°\}$ and $bw = \{0.6, 0.7, 0.8\}$ are suitable for discriminating cancer and non-cancer nuclei in HCC multispectral images. Therefore, the feature vector for representing nuclear pixel reduces 30% of utilizing all parameters.

4.6.3 Classification on single spectral band

The classification results of individual multispectral bands are presented in Table 4.1. We evaluated the performance of the system with 10-fold CV and its standard deviation in patient level. This experiment compared the classification accuracy with optimized and non-optimized Gabor parameters for discriminating normal and cancer nuclei. We conclude the result of this experiment as follows.

1. After performing optimization algorithm, the result shows that the $1^{st}, 2^{nd}$, $4^{th}, 5^{th}$ and $8^{th} - 14^{th}$ band successfully achieve high classification rate approximately over 99%. Furthermore, classification performance in $6^{th}, 7^{th}$, $13^{th}, 14^{th}$ band are around 98%.

2. The 15^{th} and 16^{th} band which is in the wavelength range 686-753 nm. have not much significant for classifying cancer and non-cancer nuclei in HCC images compare with other spectral bands.

3. Classification rates utilizing optimized Gabor parameters obtain higher performance than non-optimized for all multispectral bands.

The classification result showed that individual multispectral band contains enough information for classifying HCC and normal nuclei in high-magnification of liver tissue. In other words, the combination of multispectral bands was not necessary. By utilizing feature optimization, a small number of features are used to select the most significant features. The experimental result also showed that there are no additional advantage of using more features. It was not get more beneficial information of chromatin patterns. In addition, parameter optimization assists to improve recognition performance and reduce computational time for feature extraction and speed up the system efficiently.

Table 4.1: Comparison of classification accuracy (%) and its standard deviation between use of all of Gabor filters and optimized Gabor parameter.

band	all filters	optimization
1	92.32 ± 5.09	99.11 ± 1.03
2	88.58 ± 11.39	99.64 ± 0.31
3	88.45 ± 9.07	98.61 ± 1.98
4	90.00 ± 9.78	99.84 ± 0.25
5	87.81 ± 9.99	99.13 ± 1.06
6	87.53 ± 7.73	98.85 ± 1.16
7	94.22 ± 4.49	98.55 ± 0.98
8	97.88 ± 2.94	99.94 ± 0.09
9	93.67 ± 5.11	99.78 ± 0.31
10	88.06 ± 9.88	99.84 ± 0.31
11	95.10 ± 2.87	99.21 ± 0.79
12	94.95 ± 3.23	99.75 ± 0.61
13	95.82 ± 3.21	98.58 ± 1.27
14	93.74 ± 4.65	98.09 ± 1.43
15	92.50 ± 4.19	97.04 ± 2.25
16	90.70 ± 6.58	97.35 ± 2.74

4.6.4 Classification on color spectrum

In this experiment, we analyzed the impact of different color spectrum in visible wavelength interval for discriminating normal and cancer nuclei. The classification results and its standard deviation are shown in Table 4.2. The experimental result showed that green spectrum reported the highest classification performance (99.82%). However, blue, yellow and orange spectrum obtained classification rate 99.5% approximately and red spectrum achieved recognition rate 98.34%. These five color spectrums have similar classification performance.

Table 4.2: The wavelength interval in each color Band column is grouped multispectral bands by mapping approximately the wavelength interval for each color.

Color	Wavelength interval	Band	Classification rate (%) ± SD
Red	$\sim$ 700-635 nm.	$12^{th} - 16^{th}$	98.34 ± 2.50
Orange	$\sim$ 635-590 nm.	$10^{th} - 12^{th}$	99.51 ± 0.40
Yellow	$\sim$ 590-560 nm.	$9^{th} - 10^{th}$	99.73 ± 0.29
Green	$\sim$ 560-490 nm.	$5^{th} - 8^{th}$	99.82 ± 0.28
Blue	$\sim$ 490-450 nm.	$1^{st} - 4^{th}$	99.69 ± 0.32

4.6.5 Conclusions

This study presented a computational method for classifying HCC in multispectral images. Our propose is to analyzed based on nuclear chromatin patterns. We captures multispectral images with 100x magnification. We extracted Gabor descriptor to represent the characteristics of chromatin patterns in each nucleus. Bag of visual word model and random forest classifier were utilized to classify normal and HCC. Then, the final decision was computed based on majority voting strategy with a set of nuclei in each patient. Consequently, we performed experiment on analysis of the significant of one spectral band for distinguishing normal and cancer cell nuclei. Moreover, we applied parameter optimization algorithm to select relevant Gabor patterns which suitable for all multispectral bands at the same parameters. The experimental results shows that the use of optimized Gabor parameters improved classification accuracy of all multispectral bands comparing with using full set of Gabor parameters. For individual multispectral band analysis, most of multispectral bands have similar classification accuracy. Specifically, the $1^{st}, 2^{nd}, 4^{th}, 5^{th}$ and $8^{th} - 12^{th}$ bands achieve 99% of classification accuracies approximately. However, $3^{rd}, 6^{th}, 7^{th}$ and 13^{th} bands and $15^{th} - 16^{th}$ bands obtain 98.60% and 97%, respectively. In summary, the textures of nuclei obtained from wavelength 418-467 nm., 481-513 nm. and 548-641 nm.

are adequate to classify normal and HCC in high-magnification. Our approach shows that multispectral images provide meaningful feature in terms of classifying normal and HCC nuclei. It was also proved that nuclei texture is sufficient to classify normal and HCC.

Chapter 5

Thyroid follicular tumor classification in 3D images

5.1 Introduction

Subclassification of follicular neoplasm has been proposed to triage each patient by considering the risk of malignancy for ben-eficial treatment. The Japan Thyroid Association (JTA) categorizes indeterminate FN into three levels of risk stratification [6]. First, the favor malignant type or high risk presents the high probability of malignancy around 40-60 percents. If a patient is identified as the favor malignant type by cytological diagnosis, the patient should immediately receive its treatment. Furthermore, the borderline and the favor benign represent moderate and low risk, respectively.

Due to the limitation of 2D microscope images, we can visualize cell images in one view point. In fact, cells are in different 3D locations, and they vary in size and shape. Thus, 3D image data may provide more significant information and advantages for analysis. Moreover, 3D image data may assist pathologists to explore more details of a specific disease based on morphological properties and chromatin patterns in cancer cells. Thus, a computer aided diagnosis system based on 3D image is an additional option for pathologists to support clinical treatment.

In this study, we present a new 3D nuclei segmentation method based on unsupervised learning technique consisting of K-mean clustering and random forests

methods. Next, classification approach perform for classifying favor benign and borderline types of follicular thyroid adenoma in volumetric data. The proposed method utilizes 3D textural features in gray level co-occurrence matrix algorithm and Gabor filter banks to extract volumetric textural features of 3D segmented nuclei. Then, these texture descriptors are classified by random forest classifier. The objective of this study is to discriminate between favor benign and borderline of follicular thyroid adenoma in cytological specimens from 3D image stacks.

5.1.1 Image acquisition

The tissue samples are from Ito hospital, Tokyo, Japan where is one third of the thyroid specialist hospitals in Japan. Thus, the precision of cytologic diagnosis in thyroid is higher than other hospitals that are not specialist in analysis of thyroid nodules. Moreover, the diagnosis was evaluated with hospitals in foreign countries. The evaluated result showed that the cytologic diagnosis of thyroid in Japan, achieved higher classification accuracy than others. Therefore, our dataset that utilize in this experiment, is reliable in term of diagnosis point-of-view.

The follicular thyroid adenoma dataset were captured using the virtual slide imager [Claro, optical: 1/2 type1.6 prism, effective pixels: 1360(H) x 1024(V)] with a 3CCD digital camera. This camera system focuses on the center of nuclei in cytological specimens and automatically move up and down along depth direction with 0.25 μm for acquiring a 3D image stacks. One stack contains 41 image with 40x objective lens. Each 3D image stacks is categorized by experienced pathologists. One dataset is classified as favor benign or borderline types in follicular thyroid adenoma (FTA). This experiment contain 11 cases of favor benign and 11 cases of borderline for analysis. Figure 5.1 shows examples of the collected images. The dataset contain various kinds of background colors, different levels of image noises and inconsistent color-intensities. The 3D nuclei segmentation is a challenge task in this study.

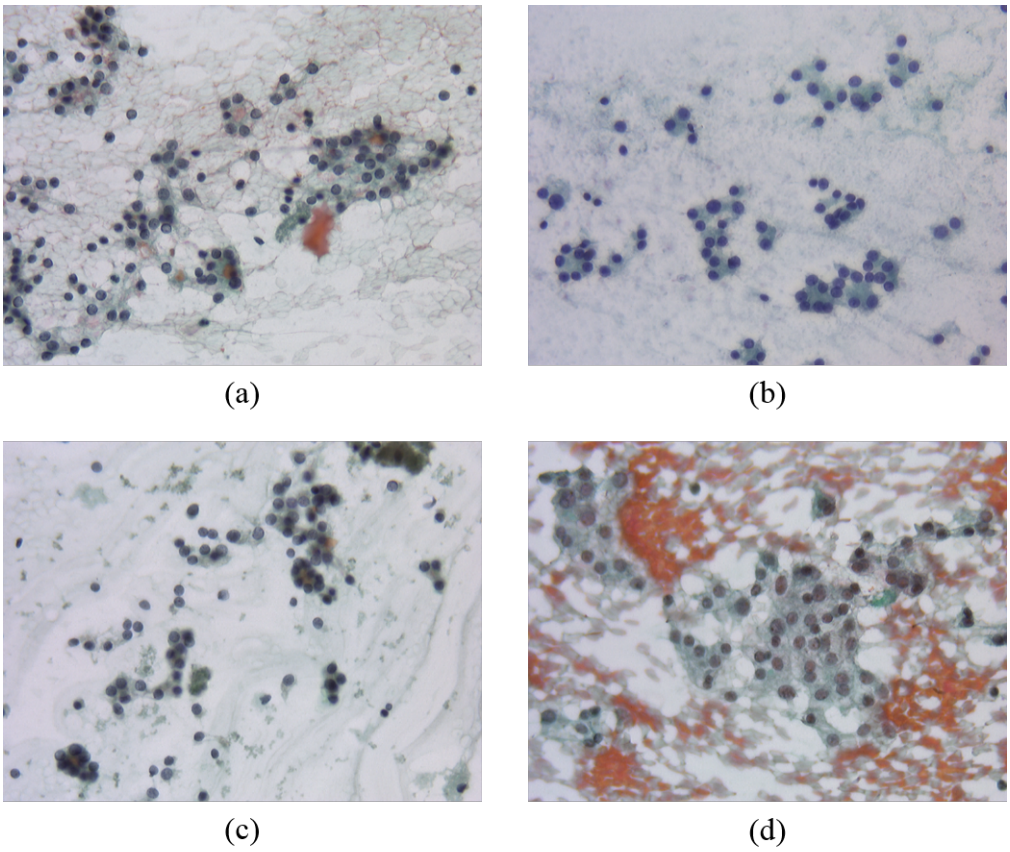

Figure 5.1: Examples of follicular thyroid adenoma images in cytological specimens. They were captured at auto focus slide of 3D stack of images. (a),(b) Favor benign type in thyroid follicular adenoma. (c),(d) Borderline type in thyroid follicular adenoma.

5.2 3D nuclei segmentation

5.2.1 Nuclei detection in 2D image slice

This study aims to detect nuclei inside images as much as possible. It is simply explained by the following steps as shown in Fig. 5.2. First, for each given 2D image slice, a preprocessing step is executed to remove some parts of cytoplasm and background areas. This removal is achieved by applying the Otsu's binarization algorithm [47] and opening morphological operations. As a result of this removal, all segmented areas are classified in two categories of individual nuclei areas and compound areas. This classification is proceeded by measureing area and circularity. In fact, the compound areas still consist of nuclei and cytoplasms. Afterwards, four image slices in individual nuclei areas and compound areas are selected to perform based on K-mean clustering. As a result of K-mean clustering, cluster centers of individual nuclei areas are utilized in the final step of 2D nuclei segmentation. On the other hand, as for the compound areas, a result of K-mean clustering gives many different clustered regions. Therefore, pixel-based classification is utilized to label each pixel in compound areas. Subsequently, the cluster centers acquired from individual nuclei areas and labeled pixels are used to indicate nuclei regions in compound areas.

In this study, pixel-based classification was performed based on unsupervised learning scheme. A classification model is provided for one stack of images. Random forest classifier [39] is used to label nuclei areas. It starts from a training step. Each pixel is represented as a six-dimensional feature vector composed of RGB and HSV color values. We separately apply K-means clustering to all pixels in each slice of a training data set to classify them into N clusters. Afterwards, all training feature vectors are labeled by considering the shortest distance from the N clusters. Most of cluster centers on a slice may be near to those on different slices in the training data. In this case, clusters on different slices that those neighboring are given a same cluster label. Thus, each data set may provide different number of labels in its training, which depend on the context of images. Actually, from our preliminary experiments, it is not good to apply the pixel-based classification to all entire data set because these images contain various

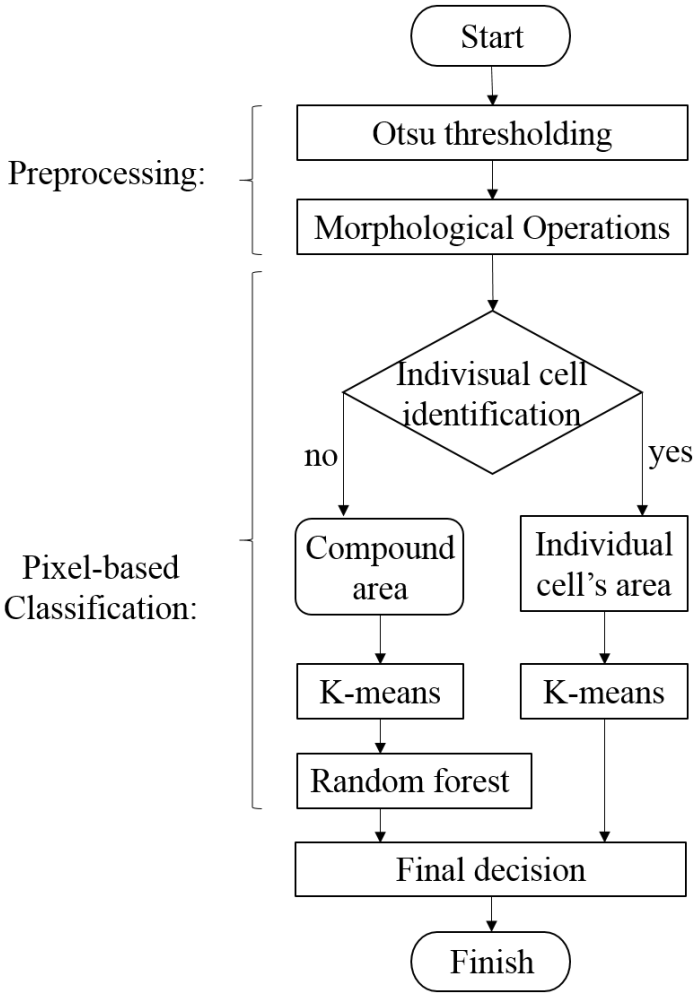

Figure 5.2: A flow chart of the proposed 2D nuclei detection

kinds of background colors, different levels of image noises, and inconsistent color-intensities. Subsequently, training features and their labels are assessed by a random forest model. The result of random forest classifier presents posterior probabilities of each feature vector. Then, we select the label presenting the maximum posterior probability as the final label of the pixel. Next, each labeled pixel will be classified as one of nuclear components if a cluster center of a labeled pixel is near to the cluster center of individual nuclei areas. Finally, these labeled pixels are refined by morphological operators. Figure. 5.4(b) shows the result of 2D nuclei segmentation.

5.2.2 3D cell construction

Referring to Fig. 5.3, a 3D nucleus volume is constructed by three main steps. The first step is to initialize a reference slice for a target nucleus. The variable k denotes a depth location of a center slice of the 3D nucleus volume in the image stacks. Furthermore, a target nuclear region in the reference slice k is indicated by R_k, which is called reference region. Neighbor slices b and t are referred to the next slice and the previous slice from reference image slice, respectively. Then, we devide the nucleus volume into top and bottom sections before applying the second and third steps to both sections. Thus a neighbor slice is referred to an upper layer counted from the reference image slice when the top section is considered. On the other hand, a neighbor image slice is a bottom layer.

In the second step, both centroids of a nuclear region in a neighbor image slice and reference image slice are considered. If the centroids of both regions are equal or slightly different, they are probably located in the same nucleus volume in a three dimensional system. However, it is necessary to validate a region in the neighbor image slice before combining it to the nuclear region in reference slice. This validation process is performed by considering four cases.

1. Similar size:

   The considered area will be merged into the area at reference slice if their sizes are equal.

2. Under segmentation:

   A region in a neighbor image slice is smaller than the region in reference slice. In this case, the region in the neighbor image slice is replaced by the region in reference slice before performing a combination.

3. Touching cells:

   If a considered region in a neighbor image slice is larger than the reference image, the considered region will be categorized as touching cell regions. Thus, we apply the Watershed transform [48] to it in order to split touching cell regions. Next, one of split regions is selected to integrate with the region in reference slice.

4. Misdetection:

   This case is preferred when no area appears in a neighbor image slice. In this case, a simulated region based on the region in reference image is created and added into the neighbor image slice for merging with R_k.

In the final step, a considered region in a neighbor image slice conforms the validate process. It is labeled by the same number of R_k. Then, the considered region of the neighbor image slice is set as R_k for obtaining a new region in the next neighbor image slice. In addition, the second and the third main steps are iterated until the top and the bottom slices are found. This process is iteratively performed for all nuclei in the dataset. The result of 3D nuclei model is shown in fig. 5.4(c) which estimated ellipsoid from major axis, minor axis and intermediate axis.

5.3 Experimental results in volumetric data

5.3.1 Implementation

We applied the proposed 3D nuclei segmentation method to FTA images as described in section 5.2. The result of 3D nuclei segmentation that is shown in Fig. 5.4. The segmented nuclei were utilized to discriminate favor benign and borderline in the classification step. In this experiment, 2D GLCM, 2D Gabor,

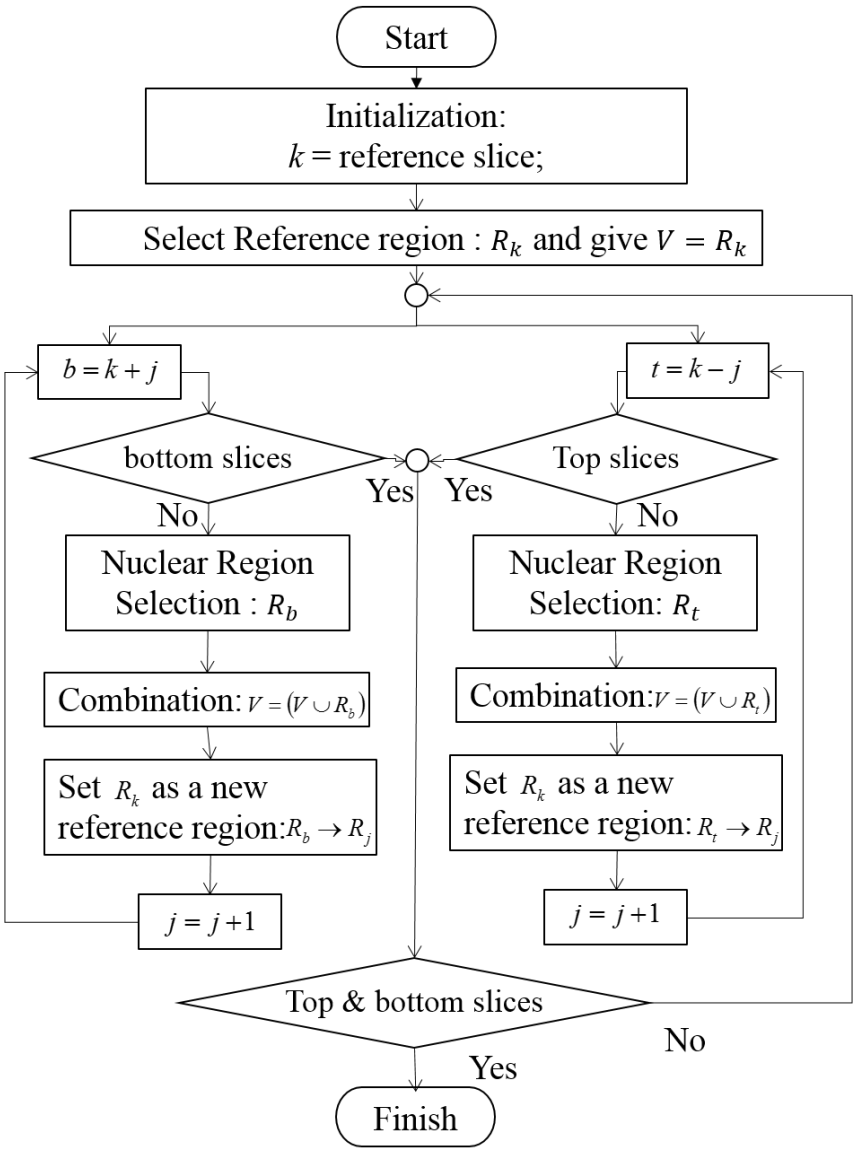

Figure 5.3: A flow chart of the proposed 2D nuclei detection

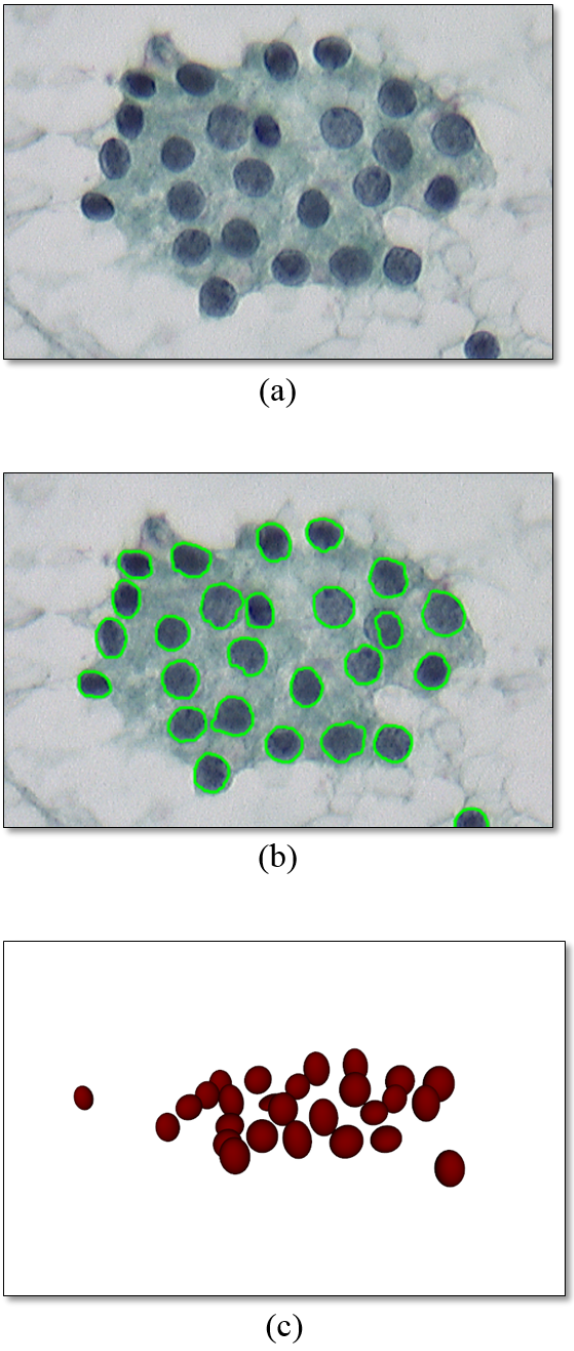

Figure 5.4: Step-bystep process of 3D nuclei segmentation. (a) An example of original image slice. (b) 2D nuclei segmentation result. (c) 3D nuclear model construction.

3D GLCM and 3D Gabor filter banks were applied to extract chromatin patterns for each 3D nuclear model over 22 cases of FTA that contain 11 cases of favor benign and 11 cases of borderline. The total of 927 nuclei are examined in this study. For GLCM parameters, we set offset $D = 1$. The 12 haralick features were extracted as described in 3.3.1.2. In Gabor filter banks, we set $\theta = \{0°, 30°, 45°, 60°, 90°, 135°\}$ in orientation, the spatial frequency bandwidth $bw = 0.9$, spatial aspect ratio $\gamma = 0.6$ and wavelength $v = 2$. This experiment extracted six different feature descriptors for each nucleus.

1. 2D GLCM extract from the center layer of image slice in four different directions including $0°, 45°, 90°, 135°$.

2. 3D GLCM method 1 compute from volumetric data considering four directions in x, y plane including $0°, 45°, 90°, 135°$.

3. 3D GLCM method 2 obtain from volumetric data in 13 directions as explained in 3.1.

4. 2D Gabor compute from the center layer of image slice.

5. 3D Gabor method 1 extract 2D Gabor filter banks from each layer of image slice and concatenate feature of each layer into 1 vector.

6. 3D Gabor method 2 calculate 3D Gabor filter banks from volumetric data.

After extracting feature descriptors, the classification procedure was performed by utilizing the BoW model and random forest classifier. The final decision was made by majority voting strategy for each image stack. Furthermore, we evaluated the performance by applying k-fold cross validation. The average accuracy over 10-fold cross validation was obtained as a result of cross-validation accuracy. In addition, six textural features were utilized to compare their performances of classification. Precision and recall are computed to evaluate the system performance. Figure 5.5 shows the overview of classification model in volumetric data.

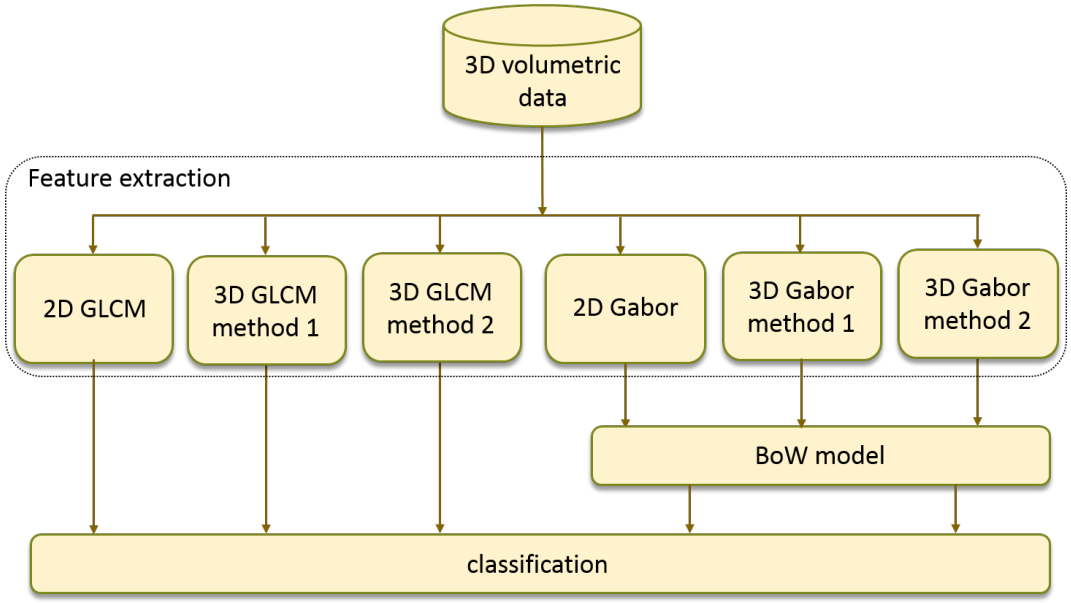

Figure 5.5: The overview of classification model in volumetric data.

Table 5.1: Comparision of classification accuracy

Texture feature	Classification accuracy(%)	Computational time(mins)	precision	recall
2D GLCM	86.36	∼0.67	1	0.78
3D GLCM method 1	90.91	∼6.39	1	0.85
3D GLCM method 2	95.45	∼23.47	1	0.92
2D Gabor	81.82	∼1.48	1	0.73
3D Gabor method 1	90.91	∼49.36	1	0.85
3D Gabor method 2	95.45	∼7.14	1	0.92

5.3.2 Classification results

The performance of classification was evaluated by using 10-fold cross validation as described in section 3.4.1. Table 5.1. shows classification accuracy of favor benign and borderline nuclei in 3D images. From the result, the use of the 3D GLCM method 2 and 3D Gabor method 2 descriptors achieved the highest classification rate 95.45 % whereas the classification based on the 3D GLCM method 1 and 3D Gabor method 1 descriptors were 90.91 %. The classification accuracy of 2D GLCM and 2D Gabor were 86.36% and 81.82%, respectively. Thus, the use of 3D GLCM method 2 and 3D Gabor method 2 descriptors are the best feature descriptor to explore volumetric data for distinguishing favor benign and borderline in FTA. However, the classification rate of 3D GLCM method 2 and 3D Gabor method 2 descriptors are same. The computational time of 3D Gabor is three times faster than 3D GLCM. In addition, the precision of all textural features is one. It means that the correct prediction rate of favor benign achieved 100%.

5.3.3 Conclusions

This study presents detection and classification systems computed in volumetric data for classifying favor benign and borderline of FTA. Pixel-based classification technique is investigated to segment nuclei in each slide by utilizing k-mean clustering and random forest classifier. Consequently, 3D nucleus model is created by combining regions among slices according to their similarities. Furthermore, We analyzed favor benign and borderline based on texture analysis of 3D shape models. We investigated the use of GLCM and Gabor descriptors to extract volumetric texture features of chromatin patterns inside a nucleus. Subsequently, the random forest classifier and majority voting strategy were performed to characterize favor benign and borderline types. Moreover, experimental results showed that the use of the 3D GLCM method 2 and 3D Gabor method 2 descriptors achieved 95.45 % of classification performance. However, the 3D GLCM method 1 and 3D Gabor method gave 90.91 % of classification accuracy. Consequently, volumetric feature descriptors probably provide more information of nuclear chromatin patterns for analysis comparing with utilizing 2D images. Specifically, The 3D Gabor method 2 descriptor compute faster than 3D GLCM method 2 descriptor.

Chapter 6

Conclusions

This thesis contains two main studies. Both of them have similar modules which consists of nuclei segmentation and classification. However, these two studies applied in different imaging technologies.

First study focused on classify HCC in multispectral images. The nuclei structure has a significant interpretation for cancer analysis in histopathological microscopic images. We analyzed hepatocellular carcinoma in 100x magnification from nuclear chromatin patterns. The multispectral imaging is a new potential technique for histopathology. It may provide an alternative to pathologists to see additional information. This study utilize multispectral images which have spatial and spectral information for nuclear analysis. The proposed framework is based on texture analysis of nuclei. The system aim to analyze the significant of multispectral bands for discriminating cancer and non-cancer nuclei. The textural features were extracted using Gabor descriptors. We present nuclei textural feature with 30 Gabor patterns at different scales and orientations. Bag-of-visual-word model with random forest classifier is employed to classify normal and cancer cells. Moreover, we remove irrelevant Gabor parameters using optimization algorithm, which achieve high recognition performance significantly. The experimental results shows that the use of optimized Gabor parameters improved classification accuracy of all multispectral bands comparing with using full set of Gabor parameters. For individual multispectral band analysis, most of multispectral bands have similar classification accuracy. Specifically, the

$1^{st}, 2^{nd}, 4^{th}, 5^{th}$ and $8^{th} - 12^{th}$ bands achieve 99% of classification accuracies approximately. However, $3^{rd}, 6^{th}, 7^{th}$ and 13^{th} bands and $15^{th} - 16^{th}$ bands obtain 98.60% and 97%, respectively. In summary, the textures of nuclei obtained from wavelength 418-467 nm., 481-513 nm. and 548-641 nm. are adequate to classify normal and HCC in high-magnification. Our approach shows that multispectral images provide meaningful feature in terms of classifying normal and HCC nuclei. It was also proved that nuclei texture is sufficient to classify normal and HCC.

Second study performed on classification of favor benign and borderline types in follicular thyroid adenoma (FTA) of volumetric data. The subclassification of follicular neoplasm (FN) plays an important role for clinical management in Japan. The diagnosis system of indeterminate thyroid nodule is intended to stratify a health risk status of patient. However, it is difficult to separate the favor benign from borderline types, and the classification process normally requires an experienced pathologist. We present a new methodology to detect nuclei in 3D image stack based on unsupervised learning. We applied pixel-based classification technique to segment nuclei in each slice by utilizing k-mean clustering and random forest classifier. Consequently, 3D nucleus model is created by combining regions among slices according to their similarities. Our proposed method can work with complex background, different levels of image noises, and inconsistent of color-intensities. Furthermore, 3D shape model is investigated to analyze sub-categories of FN between favor benign and borderline in FTA. The classification approach based on 3D nuclei model are performed for classification. We investigated the use of GLCM and Gabor descriptors to extract volumetric texture features of chromatin patterns inside nuclei. Subsequently, the random forest classifier and majority voting strategy were performed to characterize favor benign and borderline. Moreover, experimental results showed that the use of volumetric feature descriptors including 3D GLCM method 2 and 3D Gabor method 2 achieved 95.45 % of classification performance. However, the 3D GLCM method 1 and 3D Gabor method 1 descriptors gave 90.91 % of classification accuracy. The classification rate of 2D GLCM and 2D Gabor were 86.36% and 81.82%, respectively. Even though, 3D GLCM method 2 and 3D Gabor method 2 descriptors achieved same classification accuracy. However, the computational

time of 3D Gabor method 2 is three times faster than 3D GLCM method 2. Consequently, the proposed method probably helps a pathologist as a pre-screening tool.

In the future work, we will test our system with several dataset from different hospitals in order to compute performance and consistency of the system. Moreover, deep neural networks algorithm will perform to analyze cancer in our experiments since it is a popular technique and provide promising results in many applications including medical image analysis. We would like to compare classification performance with our proposed system. In second study, we would like to extend experiments focusing on 3D feature descriptors. Various kinds of volumetric feature descriptors consider to investigate in the second study for seeking the best feature descriptors which can be well represent nuclear characteristic in 3D nuclei model.

Bibliography

[1] M.N. Gurcan, L.E. Boucheron, A. Can, A. Madabhushi, N.M. Rajpoot, and B. Yener. Histopathological image analysis: A review. *Biomedical Engineering, IEEE Reviews in*, 2:147–171, 2009. 1, 2

[2] G. N. Papanicolaou. New cancer diagnosis. *Proceedings of the Third Race Betterment Conference*, pages 528–534, 1928. 2, 5

[3] Daniele Zink, Andrew H. Fischer, and Jeffrey A. Nickerson. Nuclear structure in cancer cells. *Nature reviews. Cancer*, 4(9):677–687, September 2004. ISSN 1474-175X. doi: 10.1038/nrc1430. URL http://dx.doi.org/10.1038/nrc1430. 2, 5

[4] Ahmedin Jemal, Freddie Bray, Melissa M. Center, Jacques Ferlay, Elizabeth Ward, and David Forman. Global cancer statistics. *CA: A Cancer Journal for Clinicians*, 61(2):69–90, March 2011. ISSN 1542-4863. doi: 10.3322/caac.20107. 5, 29

[5] Zubair W. Baloch, Seth Fleisher, Virginia A. LiVolsi, and Prabodh K. Gupta. Diagnosis of follicular neoplasm: A gray zone in thyroid fine-needle aspiration cytology. *Diagnostic Cytopathology*, 26(1):41–44, 2002. ISSN 1097-0339. doi: 10.1002/dc.10043. URL http://dx.doi.org/10.1002/dc.10043. 5

[6] Kakudo Kennichi, Kameyama Kaori, Hirokawa Mitsuyoshi, Katoh Ryohei, and Nakamura Hirotoshi. Subclassification of follicular neoplasms recommended by the japan thyroid association reporting system of thyroid cytology. *International Journal of Endocrinology*, (Article ID 938305), 2015. 5, 45

[7] Qingli Li, Xiaofu He, Yiting Wang, Hongying Liu, Dongrong Xu, and Fangmin Guo. Review of spectral imaging technology in biomedical engineering: achievements and challenges. *Journal of Biomedical Optics*, 18(10):100901–100901, 2013. 6

[8] A. Papadakis, E. Stathopoulos, G. Delides, K. Berberides, G. Nikiforidis, and C. Balas. A novel spectral microscope system: application in quantitative pathology. *Biomedical Engineering, IEEE Transactions on*, 50(2):207–217, Feb 2003. 6

[9] Levenson Richard, Beechem Joseph, and McNamara George. Spectral imaging in preclinical research and clinical pathology. *Analytical Cellular Pathology*, 35(5):339–361, Jan 2012.

[10] Jayakrupakar Nallala, Cyril Gobinet, Marie-Danile Diebold, Valrie Untereiner, Olivier Bouch, Michel Manfait, Ganesh Dhruvananda Sockalingum, and Olivier Piot. Infrared spectral imaging as a novel approach for histopathological recognition in colon cancer diagnosis. *Journal of Biomedical Optics*, 17(11):116013–116013, 2012. 6

[11] Jun Kong, Fusheng Wang, G. Teodoro, Yanhui Liang, Yangyang Zhu, C. Tucker-Burden, and D.J. Brat. Automated cell segmentation with 3d fluorescence microscopy images. In *Biomedical Imaging (ISBI), 2015 IEEE 12th International Symposium on*, pages 1212–1215, April 2015. doi: 10.1109/ISBI.2015.7164091. 6, 7

[12] Pedro Quelhas, Monica Marcuzzo, Ana Maria Mendona, Maria Jos Oliveira, and Aurlio C. Campilho. Cancer cell detection and invasion depth estimation in brightfield images. In *BMVC*. British Machine Vision Association, 2009. 6, 7

[13] F.A. Kruse, A.B. Lefkoff, J.W. Boardman, K.B. Heidebrecht, A.T. Shapiro, P.J. Barloon, and A.F.H. Goetz. The spectral image processing system (sips)interactive visualization and analysis of imaging spectrometer data. *Remote Sensing of Environment*, 44(23):145 – 163, 1993. ISSN 0034-4257. Airbone Imaging Spectrometry. 7

[14] Chein-I Chang. Spectral information divergence for hyperspectral image analysis. In *Geoscience and Remote Sensing Symposium, 1999. IGARSS '99 Proceedings. IEEE 1999 International*, volume 1, pages 509–511 vol.1, 1999. 7

[15] Yana Guan, Qingli Li, Yiting Wang, Hongying Liu, and Ziqiang Zhu. Pathological leucocyte segmentation algorithm based on hyperspectral imaging technique. *Optical Engineering*, 51(5):053202–1–053202–7, 2012. 7

[16] Xuqing Wu, M. Amrikachi, and S.K. Shah. Embedding topic discovery in conditional random fields model for segmenting nuclei using multispectral data. *Biomedical Engineering, IEEE Transactions on*, 59(6):1539–1549, June 2012. ISSN 0018-9294. 7

[17] Ningning Guo, Libo Zeng, and Qiongshui Wu. A method based on multispectral imaging technique for white blood cell segmentation. *Computers in Biology and Medicine*, 37(1):70 – 76, 2007. ISSN 0010-4825. 7, 9

[18] Mat Straka, Alexandra La Cruz, Arnold Kchl, Milo rmek, Dominik Fleischmann, and Eduard Grller. 3d watershed transform combined with a probabilistic atlas for medical image segmentation. In *Proceedings of MIT 2003*, pages 1–8, 2003. 7

[19] H. Kalkan, M. Nap, R. P. W. Duin, and M. Loog. Automated classification of local patches in colon histopathology, Nov 2012. ISSN 1051-4651. 8

[20] Rahmadwati, G. Naghdy, M. Ros, C. Todd, and E. Norahmawati. Cervical cancer classification using gabor filters. *Healthcare Informatics, Imaging and Systems Biology (HISB), 2011 First IEEE International Conference on*, pages 48–52, July 2011. doi: 10.1109/HISB.2011.15. 8

[21] H. Peng, Fulmi Long, and C. Ding. Feature selection based on mutual information criteria of max-dependency, max-relevance, and min-redundancy. *Pattern Analysis and Machine Intelligence, IEEE Transactions on*, 27(8): 1226–1238, Aug 2005. 8

[22] Monalisa Mandal and Anirban Mukhopadhyay. An improved minimum redundancy maximum relevance approach for feature selection in gene expression data. *Procedia Technology*, 10(0):20 – 27, 2013. First International Conference on Computational Intelligence: Modeling Techniques and Applications (CIMTA) 2013. 8

[23] Xin Qi, Fuyong Xing, David J. Foran, and Lin Yang. Comparative performance analysis of stained histopathology specimens using rgb and multispectral imaging, 2011. 8, 9

[24] J.M. Sotoca, F. Pla, and J.S. Sanchez. Band selection in multispectral images by minimization of dependent information. *Systems, Man, and Cybernetics, Part C: Applications and Reviews, IEEE Transactions on*, 37(2):258–267, March 2007. 9

[25] J.M. Sotoca, F. Pla, and A.C. Klaren. Unsupervised band selection for multispectral images using information theory. In *Pattern Recognition, 2004. ICPR 2004. Proceedings of the 17th International Conference on*, volume 3, pages 510–513 Vol.3, Aug 2004.

[26] Adolfo Martnez-Us, Filiberto Pla, Pedro Garca-Sevilla, and J.M. Sotoca. Automatic band selection in multispectral images using mutual information-based clustering. In JosFrancisco Martnez-Trinidad, JessAriel Carrasco Ochoa, and Josef Kittler, editors, *Progress in Pattern Recognition, Image Analysis and Applications*, volume 4225 of *Lecture Notes in Computer Science*, pages 644–654. Springer Berlin Heidelberg, 2006. ISBN 978-3-540-46556-0. doi: 10.1007/11892755_67.

[27] S. De Backer, P. Kempeneers, W. Debruyn, and P. Scheunders. A band selection technique for spectral classification. *Geoscience and Remote Sensing Letters, IEEE*, 2(3):319–323, July 2005.

[28] Baofeng Guo, S.R. Gunn, R.I. Damper, and J.D.B. Nelson. Band selection for hyperspectral image classification using mutual information. *Geoscience and Remote Sensing Letters, IEEE*, 3(4):522–526, Oct 2006. 9

[29] Qiongshui Wu, Libo Zeng, Hengyu Ke, Hong Zheng, Xijian Gao, and Diancheng Wang. A multispectral imaging analysis system for early detection of cervical cancer, 2005. 9

[30] A. Gertych, G. Galliano, S. Bose, and D. L. Farkas. Automatic recognition of abnormal cells in cytological tests using multispectral imaging, 2010. 9

[31] H. Irshad, A. Gouaillard, L. Roux, and D. Racoceanu. Multispectral band selection and spatial characterization: Application to mitosis detection in breast cancer histopathology. *Computerized Medical Imaging and Graphics*, 38(5):390 – 402, 2014. doi: http://dx.doi.org/10.1016/j.compmedimag.2014.04.003. 9

[32] Balasubramanian Gopinath and Natesan Shanthi. Computer-aided diagnosis system for classifying benign and malignant thyroid nodules in multi-stained fnab cytological images. *Australasian Physical & Engineering Sciences in Medicine*, 36(2):219–230, 2013. doi: 10.1007/s13246-013-0199-8. 10

[33] Wei Wang, John A. Ozolek, and Gustavo K. Rohde. Detection and classification of thyroid follicular lesions based on nuclear structure from histopathology images. *Cytometry Part A*, 77A(5):485–494, 2010. ISSN 1552-4930. 10

[34] Chanho Jung and Changick Kim. Impact of the accuracy of automatic segmentation of cell nuclei clusters on classification of thyroid follicular lesions. *Cytometry Part A*, 85(8):709–718, 2014. ISSN 1552-4930. 10

[35] Angel Cruz-Roa, Ajay Basavanhally, Fabio Gonzlez, Hannah Gilmore, Michael Feldman, Shridar Ganesan, Natalie Shih, John Tomaszewski, and Anant Madabhushi. Automatic detection of invasive ductal carcinoma in whole slide images with convolutional neural networks, 2014. URL http://dx.doi.org/10.1117/12.2043872. 11

[36] Dan C. Cireşan, Alessandro Giusti, Luca M. Gambardella, and Jürgen Schmidhuber. *Medical Image Computing and Computer-Assisted Intervention – MICCAI 2013: 16th International Conference, Nagoya, Japan,*

September 22-26, 2013, Proceedings, Part II, chapter Mitosis Detection in Breast Cancer Histology Images with Deep Neural Networks, pages 411–418. Springer Berlin Heidelberg, Berlin, Heidelberg, 2013. ISBN 978-3-642-40763-5. doi: 10.1007/978-3-642-40763-5_51. URL http://dx.doi.org/10.1007/978-3-642-40763-5_51. 11

[37] Antonis Daskalakis, Spiros Kostopoulos, Panagiota Spyridonos, Dimitris Glotsos, Panagiota Ravazoula, Maria Kardari, Ioannis Kalatzis, Dionisis Cavouras, and George Nikiforidis. Design of a multi-classifier system for discriminating benign from malignant thyroid nodules using routinely he-stained cytological images. *Computers in Biology and Medicine*, 38(2):196 – 203, 2008. ISSN 0010-4825. doi: http://dx.doi.org/10.1016/j.compbiomed.2007.09.005. URL http://www.sciencedirect.com/science/article/pii/S0010482507001588. 11

[38] Lee Chin Omar Falou William T. Tran Frances C. Wright Sonal Gandhi Martin J. Yaffe Ali Sadeghi-Naini, Eric Vorauer and Gregory J. Czarnota. Early detection of chemotherapy-refractory patients by monitoring textural alterations in diffuse optical spectroscopic images. *Medical Physics*, 42(11): 61306146, 2015. 11

[39] Leo Breiman. Random forests. *Mach. Learn.*, 45(1):5–32, October 2001. 16, 25, 48

[40] Robert M. Haralick, Stanley R. Sternberg, and Xinhua Zhuang. Image analysis using mathematical morphology. *Pattern Analysis and Machine Intelligence, IEEE Transactions on*, PAMI-9(4):532 –550, july 1987. ISSN 0162-8828. doi: 10.1109/TPAMI.1987.4767941. 18

[41] Texture analysis of medical images. *Clinical Radiology*, 59(12):1061 – 1069, 2004. 21

[42] N. Petkov and P. Kruizinga. Computational models of visual neurons specialised in the detection of periodic and aperiodic oriented visual stimuli: bar and grating cells. *Biological Cybernetics*, 76(2):83–96, 1997. 21

[43] Arati S. Kurani, Dong hui Xu, Jacob Furst, and Daniela Stan Raicu. Raicu . co-occurrence matrices for volumetric data. the. In *7th IASTED International Conference on Computer Graphics and Imaging, Kauai*, 2004. 22

[44] Fuan Tsai, Chun-Kai Chang, Jian-Yeo Rau, Tang-Huang Lin, and Gin-Ron Liu. 3d computation of gray level co-occurrence in hyperspectral image cubes. In *Proceedings of the 6th International Conference on Energy Minimization Methods in Computer Vision and Pattern Recognition*, EMMCVPR'07, pages 429–440, Berlin, Heidelberg, 2007. Springer-Verlag. 22

[45] R. M. Haralick. Statistical and structural approaches to texture. *Proceedings of the IEEE*, 67(5):786–804, May 1979. 22

[46] Robert M. Haralick and Linda G. Shapiro. *Computer and Robot Vision*. Addison-Wesley Longman Publishing Co., Inc., Boston, MA, USA, 1st edition, 1992. 22

[47] N. Otsu. A threshold selection method from gray-level histograms. *IEEE Transactions on Systems, Man and Cybernetics*, 9(1):62–66, January 1979. 35, 48

[48] Xiaodong Yang, Houqiang Li, and Xiaobo Zhou. Nuclei Segmentation Using Marker-Controlled Watershed, Tracking Using Mean-Shift, and Kalman Filter in Time-Lapse Microscopy. *Microscopy*, 53(11):2405–2414, 2006. 51

Publication List

Journal Articles

1. **Oranit Boonsiri**, Kiyotada Washiya, and Hiroshi Nagahashi. 3D gray level co-occurrence matrix based classification of favor benign and borderline types in follicular neoplasm images, *Journal of Biosciences and Medicines*, vol. 4, 51-56, March 2016.

2. **Oranit Boonsiri**, Chamidu Atupelage, Hiroshi Nagahashi, Kota Aoki, Fumikazu Kimura, and Masahiro Yamaguch. Multispectral Band Analysis: Application on the Classification of Hepatocellular Carcinoma Cells in High-Magnification Histopathological Images, *Journal of Cytology and Histology*, S3:006, 2015.

International Conferences

1. **Oranit Boonsiri**, Kiyotada Washiya, and Hiroshi Nagahashi. 3D gray level co-occurrence matrix based classification of favor benign and borderline types in follicular neoplasm images, *The second international conference on pathology*, Los Angeles, USA, March, 2016.

2. **Oranit Boonsiri**, Chamidu Atupelage, Hiroshi Nagahashi, Kota Aoki, Fumikazu Kimura, and Masahiro Yamaguch. Significance of multispectral band for classification of cancer cells in hepatocellular carcinoma from histophatology images using gabor descriptor, *The fourth international workshop on image electronics and visual computing*, Samui, Thailand, October, 2014.

Domestic Conferences

1. **Oranit Boonsiri**, Chamidu Atupelage, Hiroshi Nagahashi, Kota Aoki, Fumikazu Kimura, and Masahiro Yamaguch. Detection and Classification of Hepatic Cancer from Multispectral Histopathology Images, In *IIEEJ* 41^{st} *Media Computing Conference*, Aomori, Japan, June 2013.